CM² MAGAZINE

第 54 期

南方科技大学海洋磁学中心

https://cm2.sustech.edu.cn/

创刊词

海洋是生命的摇篮，是文明的纽带。地球上最早的生命诞生于海洋，海洋里的生命最终进化成了人类，人类的文化融合又通过海洋得以实现。人因海而兴。

人类对海洋的探索从未停止。从远古时代美丽的神话传说，到麦哲伦的全球航行，再到现代对大洋的科学钻探计划，海洋逐渐从人类敬畏崇拜幻想的精神寄托演变成可以开发利用与科学研究的客观存在。其中，上个世纪与太空探索同步发展的大洋科学钻探计划将人类对海洋的认知推向了崭新的纬度：深海（deep sea）与深时（deep time）。大洋钻探计划让人类知道，奔流不息的大海之下，埋藏的却是亿万年的地球历史。它们记录了地球板块的运动，从而使板块构造学说得到证实；它们记录了地球环境的演变，从而让古海洋学方兴未艾。

在探索海洋的悠久历史中，从大航海时代的导航，到大洋钻探计划中不可或缺的磁性地层学，磁学发挥了不可替代的作用。这不是偶然，因为从微观到宏观，磁性是最基本的物理属性之一，可以说，万物皆有磁性。基于课题组的学科背景和对海洋的理解，我们对海洋的探索以磁学为主要手段，海洋磁学中心因此而生。

海洋磁学中心，简称 CM^2，一为其全名“Centre for Marine Magnetism”的缩写，另者恰与爱因斯坦著名的质能方程 $E = MC^2$ 对称，借以表达我们对科学巨匠的敬仰和对科学的不懈追求。

然而科学从来不是单打独斗的产物。我们以磁学为研究海洋的主攻利器，但绝不仅限于磁学。凡与磁学相关的领域均是我们关注的重点。为了跟踪反映国内外地球科学特别是与磁学有关的地球科学领域的最新研究进展，海洋磁学中心特地主办 CM^2 Magazine，以期与各位地球科学工作者相互交流学习、合作共进！

“海洋孕育了生命，联通了世界，促进了发展”。 21 世纪是海洋科学的时代，由陆向海，让我们携手迈进中国海洋科学的黄金时代！

目 录

磁学演绎

第 44 章 生物来源的磁性矿物

在许多动物体 [Kirschvink and Gould, 1981; Wiltschko and Wiltschko, 2005]，例如鸟类 [Beason et al., 1995; Altringham, 1996]、蝙蝠 [Tian et al., 2010]、蜜蜂 [Kirschvink and Kirschvink, 1991]、鱼类 [Moore et al., 1990]、白蚁 [Maher, 1998; Alves et al., 2004] 和人类 [e.g., Kirschvink et al., 1992; Fuller et al., 1995; Dubiel et al., 1999] 中都发现了生物成因的磁性矿物。生物磁学材料（如铁蛋白）也在医学方面有重要的作用。我们在此主要介绍与环境磁学研究相关的生物体。

生物过程通过两种主要方式产生磁性矿物，即生物控制矿化（BCM）和生物诱导矿化（BIM） [Moskowitz, 1995; Bazylinski and Frankel, 2004; Faivre and Schüler, 2008; Kopp and Kirschvink, 2008]。生物诱导矿化可以产生很多种铁氧化物，例如磁铁矿、针铁矿、纤铁矿和水铁矿，并且它们的粒径分布很宽 [Hesse and Stolz, 1999; Egli, 2004a, b]。细颗粒胶黄铁矿也可以通过生物诱导矿物过程产生，主要是 SP 和一小部分的 SD 颗粒 [Watson et al., 2000]。磁颗粒粒径分布较宽意味着生物诱导磁性矿物即使主导了磁性组分，也很难被识别。相反，生物控制矿化机制可以产生化学计量的纯的并且形态学上独特的 SD 磁铁矿 [Blakemore, 1975; Stolz et al., 1986; Pósfai et al., 2006; Li et al., 2010] (图 1) 或者胶黄铁矿颗粒 [Mann et al., 1990; Bazylinski et al., 1993; Kasama et al., 2006]。这些颗粒被趋磁细菌用于沿着地磁场线在好氧-缺氧过渡区周围和以下寻找氧化还原边界[Bazylinski et al., 1993; Kopp and Kirschvink, 2008; Moskowitz et al., 2008]。关于趋磁细菌的最初研究起源于探索化石磁小体作为沉积物中天然剩磁的载体 [Kirschvink, 1983; Stolz et al., 1986; Snowball, 1994]。鉴于趋磁细菌和特定氧化还原条件的关系，化石磁小体可以记录环境的变化[Oldfield et al., 1992; Lean and McCave, 1998; Yamazaki and Kawahata, 1998; Dinarès-Turell et al., 2003; Faivre et al., 2008; Kopp and Kirschvink, 2008; Li et al., 2010; Roberts et al., 2011b; Yamazaki, 2012]和过去生物的活动 [Arató et al., 2005; Kopp and Kirschvink, 2008; Jiménez-López et al., 2010]。

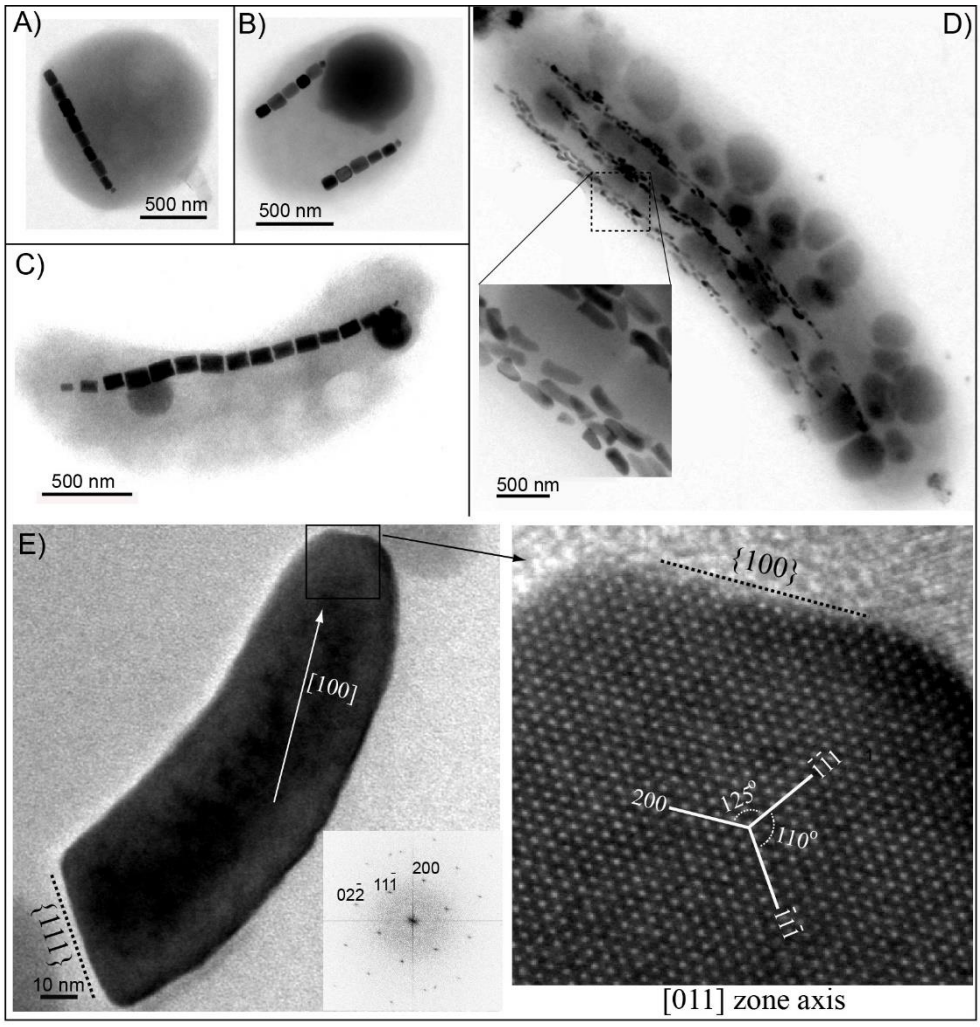

图 1. 来自北京密云水库的趋磁细菌以及它们细胞内的磁小体. (A)棱镜状磁小体单链构成的趋磁球菌；（B）双链趋磁球菌；（C）单链趋磁弧菌；（D）子弹头形磁小体构成的多链趋磁杆菌（MYR-1）；（E）MYR-1 中子弹头磁小体的高分辨率投射电子显微镜. 不像棱镜状和立方八面体磁铁矿磁小体沿[111]面拉长定向，子弹头磁小体主要沿磁铁矿的[100]面拉长[Li et al., 2010, and unpublished data].

海洋沉积物中，从浅海一直到 4500 米深处都可以发现趋磁细菌的踪迹[Stoltz et al., 1986; Petermann and Bleil, 1993; Hesse, 1994; Hesse and Stoltz, 1999; Bazylinski and Frankel, 2004; Housen and Moskowitz, 2006; Faivre and Schüler, 2008; Kopp and Kirschvink, 2008]。除了现代海洋沉积物中磁小体有较大潜在含量外，关于磁小体化石主导古海洋沉积物磁性的报道并不多见，因为小颗粒极有可能在埋藏过程中被溶解 [e.g., Schwartz et al., 1997; Kopp and Kirschvink, 2008]。对第四纪海洋沉积物的研究显示，磁铁矿的粒径和含量变化可以携带冰期间冰期循环

中真正的同生沉积信号。在冰期时，底层水氧化作用的降低和有机碳供给的增加可能导致冰期孔隙水中含氧量的降低，生物成因磁铁矿也会随之降低 [Hesse, 1994; Yamazaki and Kawahata, 1998; Yamazaki, 2012]。大量研究也表明，相对于拉长型的磁小体，等轴的磁小体更适应于有机碳供给降低的时期 [Hesse, 1994; Lean and McCave, 1998; Dinarès-Turell et al., 2003]，然而也有研究显示出相反的结果[Lean and McCave, 1998]。总体来说，生物磁铁矿是在沉积物-水界面或其上生成的。然而，一些研究显示，如果还原环境使得有氧-缺氧过渡带移至沉积物-水界面之下，生物成因磁铁矿也可以生成。在这种情况下，磁小体化石可以携带比寄主沉积物更年轻的生物（地球）化学剩磁 [Tarduno and Wilkison, 1996; Tarduno et al., 1998; Abrajevitch and Kodama, 2011]。生物磁铁矿的保存指示了成岩环境，在这种环境中，生物磁铁矿可以在不间断的沉积中得到保存，并通常指示了沉积速率的增加或者是第四纪冰期间冰期循环中古生产力的变化 [Tarduno et al., 1998; Abrajevitch and Kodama, 2011]。即便如此，解释古磁小体化石的最主要的障碍仍是将磁小体化石的生成和保存信号分开 [Hesse and Stoltz, 1999]。

通常，在第四纪以前的沉积物中都缺乏生物成因的磁铁矿，但古新世-始新世最暖期（PETM）沉积物是一个例外。PETM 是早期全球变暖的最好代表[Zachos et al., 2001]。许多研究人员证实了在中大西洋美国大陆边缘浅海 PETM 沉积物中广泛存在着生物成因的磁铁矿[Lippert and Zachos, 2007; Kopp et al., 2007, 2009; Schumann et al., 2008]。Kopp et al. [2009] 推测，由于全球温度和湿度的增加，大陆架有机碳供给和陆源供给随之增加，有利于趋磁细菌的增殖，因而磁小体化石更容易在大型热带河流的河口处累积。磁小体化石和 PETM 的联系指示了一个次氧化成岩环境的厚层所建立的对磁小体化石的保存效应，而这种保存效应的建立正是由于沉积速率短暂增加将 PETM 沉积物和上覆硫化沉积物分离[Dickens, 2008; Kopp et al., 2009]。如果事实真是如此，磁小体化石的丰度就不能作为细菌生产力的可靠指标。相反，它们更像是代表了特定的、短暂的成岩环境。在较深的沉积中，铁元素是浮游植物主要受限制的营养元素。粉尘所携带的铁元素为磁铁矿磁小体化石保存提供了最适宜的环境 [Roberts et al., 2011b; Larrasoaña et al., 2012]。这种铁肥可以增加初级生产力和对海底有机碳的输出，因而创造一个温和的铁还原环境，将铁从粉尘最活跃的组分中释放，从而保障磁小体化石的生长

和保存。关于磁小体化石与风成粉尘相联系的众多报道说明[Bloemendal et al., 1992; Yamazaki and Ioka, 1997b; Dinarès-Turell et al., 2003; Yamazaki, 2009; Abrajevitch and Kodama, 2011]，在趋磁细菌和粉尘所供应的铁肥之间存在一个广泛的联系，虽然这种机制仅仅适用于缺少铁的海洋环境中 [Roberts et al., 2011b]。

在缺氧-有氧带以下的缺氧环境中，有大量关于胶黄铁矿磁小体的报道[Bazylinski et al., 1993; Vasiliev et al., 2008; Kopp and Kirschvink, 2008; Lefèvre et al., 2011]。但在地质记录中，关于胶黄铁矿磁小体化石的报道却很少。胶黄铁矿磁小体化石被认为会产生延时的生物（地球）化学剩磁，但在快速沉积的沉积物中，OATZ 带存在于水体中或者沉积物上层，这时，这种延时作用是很小的。

以往的研究在全世界范围内湖泊和沼泽的沉积物-水界面边界报道了趋磁细菌的存在 [Hawthorne and McKenzie, 1993; Peck and King, 1996; Hesse and Stolz, 1999]。在温带或半干旱气候带的大多数湖泊中，由于生物生产率和沉积速率通常都比较高，沉积过程中的缺氧环境阻碍了磁小体化石的保存 [Hesse and Stolz, 1999]。而对于许多高纬度湖泊，其集水区较小，地势低平，植被覆盖面积小，季节性冰盖小，这些因素限制了陆源的输入，为晚更新世和全新世沉积物中磁小体化石的形成和保存提供了有利的条件 [Snowball, 1994; Nolan et al., 1999; Snowball et al., 1999, 2002; Paasche et al., 2004; Paasche and Løvlie, 2011]。因此，这些湖泊中磁小体化石的变化携带了重要的冰期间冰期季节尺度的古环境信息，但迄今为止，关于气候和磁小体化石丰度之间联系的机制还有待进一步解决[Paasche and Løvlie, 2011]。

文献速递

1. 北纬 38 度西北太平洋冰筏碎屑揭示了西伯利亚东北部冰盖多期次冰盖变化

翻译人：仲义 zhongy@sustech.edu.cn

A.P. McCarron, G.R. Bigg, H. Brooks, et al., ***Northwest Pacific ice-rafted debris at 38°N reveals episodic ice-sheet change in late Quaternary Northeast Siberia [J] Earth and Planetary Science Letters,*** *2020, 553, 116650.*
https://doi.org/10.1016/j.epsl.2020.116675

摘要：在开放的西北太平洋的冰筏碎屑（IRD）记录表明，在晚第四纪东北海岸有大量的冰川存在。然而，由于陆上和海上记录的缺乏，冰川期和冰消期的规模和时间仍然存在争议。现有的 IRD 数据表明，在氧同位素 3 期中晚期至少发生了一次快速变化事件，反映出海因里希事件期间的劳伦冰盖的大规模崩塌。但在晚第四纪是否还发生过类似规模的事件仍然不清楚。作者基于 ODP1207A 孔（37.79° N, 162.75° E）160 千年以来的 IRD 序列、浮游有孔虫数量及底栖氧同位素、放射性年代和火山灰确定的年代框架，揭示了其 IRD 含量较低但是出现多期次通量变化。作者认为西北太平洋冰川冰山至少在第四纪最后两个冰期期间向更南扩散，冰山从西伯利亚东北部搬运到亚极地与亚赤道太平洋的过渡地带，并位于亚北极锋面以南。在末次冰期中 1207A IRD 结果出现的多期次特征，利用气候-冰山耦合模型显示来自勘察加-科利亚克海岸的冰通量间歇性增强，其潜在来源是鄂霍次克海海岸。这些发现支持了这样一种假设：在西伯利亚东北部的最后一次冰期，特别是在最后一次冰期的早期，存在一个变化但范围广泛的冰块，且独立于北美和欧亚大陆之间的冰块。与之形成强烈对比的是，在倒数第二个冰期氧同位素 6 期的大部分时间内 IRD 是缺失的，这表明在最后两个冰期之间，东北西伯利亚的冰覆盖可能存在很大差异。。

ABSTRACT: The ice-rafted-debris (IRD) record of the open Northwest Pacific points towards the existence of substantial glacial ice on the Northeast Siberian coast during the late Quaternary. However, the scale and timing of glaciation and de-glaciation remains controversial due to the dearth of both onshore and offshore records. Existing IRD data suggests at least one event of dynamic and abrupt change during mid-late Marine Isotope Stage (MIS 3) which mimics the massive collapse of

the Laurentide ice sheet during Heinrich Events. It is uncertain whether other events of this magnitude occurred during the late Quaternary. Here we present a ~160,000 yr IRD series, planktic foraminiferal counts and an age model, derived from a benthic δ18O curve, radiocarbon dates and tephrochronology, from core ODP 1207A (37.79◦N, 162.75◦E), revealing the presence of low but episodic flux of IRD. We conclude that glacial Northwest Pacific icebergs spread further south than previously thought, with icebergs emanating from Northeast Siberia being transported to the transition region between the subpolar and subtropical waters, south of the subarctic front during at least the Quaternary's last two glacial periods. The episodic nature of the 1207A IRD record during the last glacial, combined with coupled climate-iceberg modelling, suggests occasional times of much enhanced ice flux from the Kamchatka-Koryak coast, with other potential sources on the Sea of Okhotsk coast. These findings support the hypothesis of a variable but extensive ice mass during the last glacial over Northeast Siberia, particularly early in the last glacial period, behaving independently of North American and Eurasian ice masses. In strong contrast, IRD was absent during much of the penultimate glacial Marine Isotope Stage (MIS) 6 suggesting the possibility of very different Northeast Siberian ice coverage between the last two glacial periods.

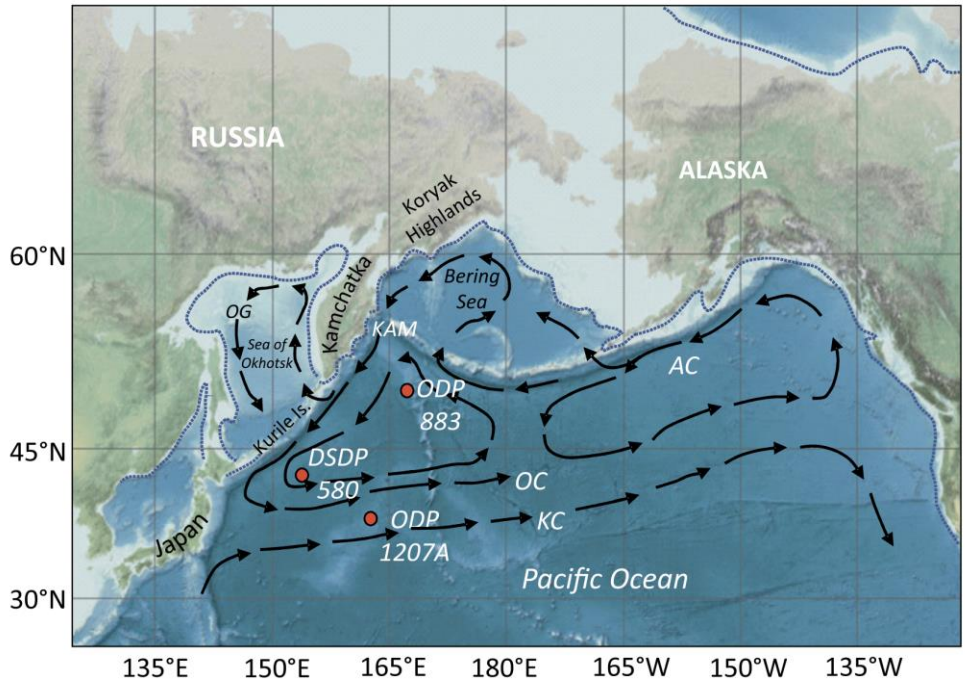

Figure 1. Study Region. Core sites mentioned in this study are shown by the labelled red markers. Major last glacial surface ocean current patterns are shown by arrows and labelled as follows: AC = Alaska

Current; KAM = Kamchatka Current; KC = Kuroshio Current; OC = Oyashio Current; OG = Okhotsk Gyre. The dotted line shows the LGM coastline. The shallower region of the Meiji Drift is located between the KAM and the site of ODP883. (For interpretation of the colours in the figure(s), the reader is referred to the web version of this article.)

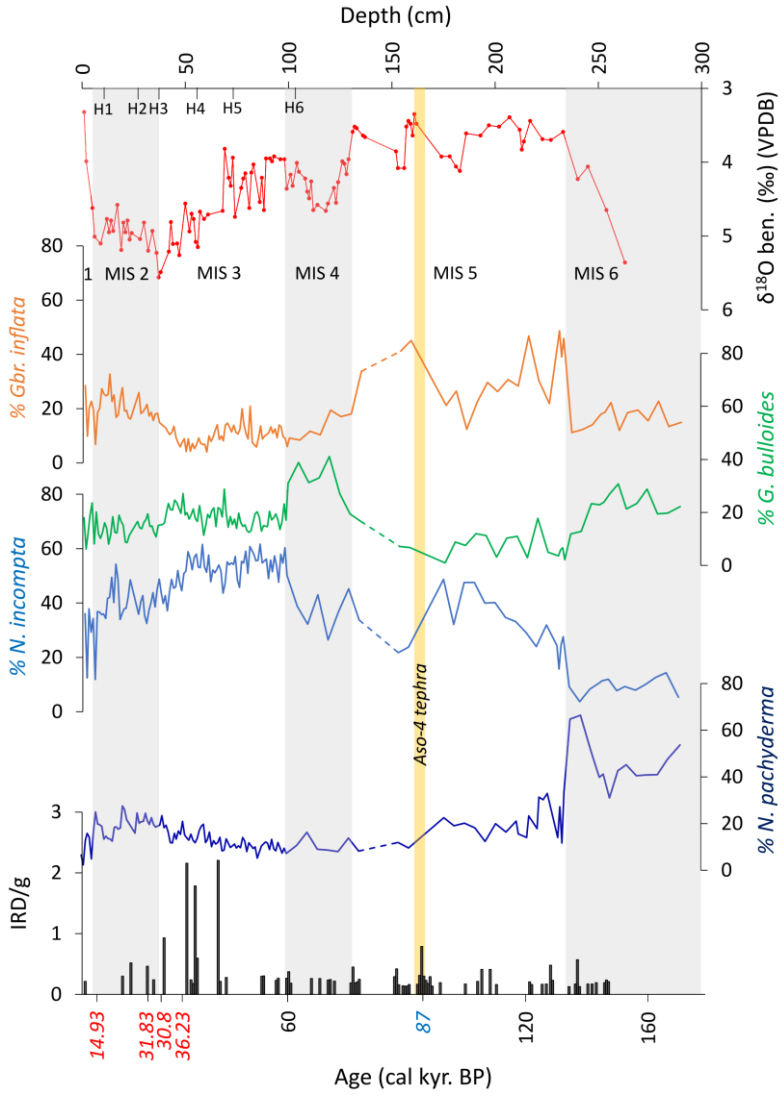

Figure 2. δ18O, IRD and relative abundances of the four most common planktic foraminifera species in the top 3 m of ODP 1207A. Dashed lines denote a hiatus in the sediment (see section 2.1). Dates in red are calibrated median probability 14C dates (see Table 1). The blue date, marked by the yellow bar denotes the Aso-4 tephra. Dates in black were extrapolated from the δ18O stratigraphy, 14C and tephra ages, as described in section 3.1. Marine Isotope Stages are marked by alternating grey bars. Approximate timings of Atlantic Heinrich Events are shown by H1-H6 (Hemming, 2004). The absence of an IRD bar is a zero count, as 1 cm interval IRD recording extended to 300 cm.

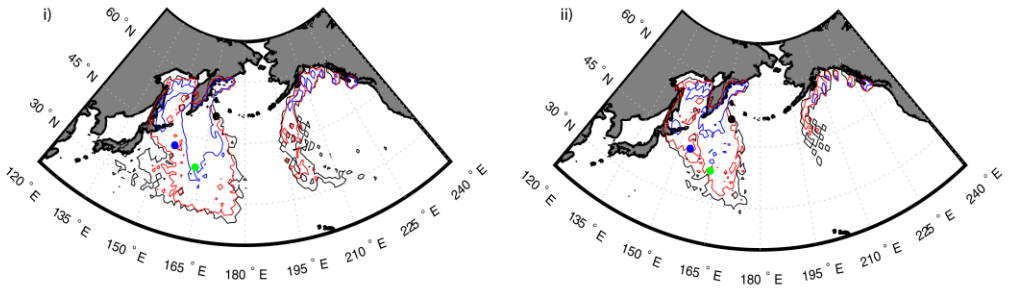

Figure 3. Iceberg density maps for:: i) maximal flux simulation and ii) typical iceberg flux simulation. Contours are number of icebergs entering a 1 × 1o square in a 10 yr period – 1 (black); 10 (red); 100 (blue); 1000 (black). ODP site 1207 shown by a green dot, DSDP 580 is shown by a blue dot, and ODP 883 is shown by a black dot.

2. 评估冰期冰消期改变大气 CO2 的假说：碳呼吸作用和通风变化

翻译人：蒋晓东 jiangxd@sustech.edu.cn

*Stott L D, Shao J, Yu J M, et al .**Evaluating the glacial-deglacial carbon respiration and ventilation change hypothesis as a mechanism for changing atmospheric CO2** [J]. **Geophysical Research Letters**, 2020.*

https://doi.org/10.1002/essoar.10504708.1

摘要：末次冰期聚集在深海的超量的呼吸碳因通风作用增强而使释放更多 CO_2，该观点是关于末次冰期终止时 pCO_2 升高盛行的假说。近期研究认为有可能是冰期时海洋中较低的氧气引起。在末次冰期最冷时氧气亏损的尺度约为 100-140 μmol/kg，因为呼吸作用与溶解态无机碳的$\delta^{13}C$ 相耦合，该氧气亏损的尺度可使溶解态无机碳的$\delta^{13}C$ 相较于表层水降低约 1‰。延长的扣呼吸碳押作用也能使深海中 ^{14}C 的量降低。本研究揭示太平洋深层水溶解态无机碳的$\delta^{13}C$ 相较于表层水并未降低，在晚冰期$\Delta^{14}C$ 仅低了约 50‰。对冰消期通风变化的假说进行模型模拟研究，结果显示溶解态无机碳的$\delta^{13}C$、$\Delta^{14}C$、$\varepsilon^{14}C$ 大幅增加，而这些结果并未实测到。

ABSTRACT: The prevailing hypothesis to explain pCO_2 rise at the last glacial termination calls upon enhanced ventilation of excess respired carbon that accumulated in the deep sea during the glacial. Recent studies argue lower $[O_2]$ in the glacial ocean is indicative of increased carbon respiration. The magnitude of $[O_2]$ depletion was 100-140 μmol/kg at the glacial maximum. Because respiration is coupled to $\delta^{13}C$ of dissolved inorganic carbon (DIC), $[O_2]$ depletion of 100-140 μmol/kg from carbon respiration would lower deep water $\delta^{13}C_{DIC}$ by ~ 1‰ relative to surface water. Prolonged sequestration of respired carbon would also lower the amount of ^{14}C in the deep sea. We show that Pacific Deep Water $\delta^{13}C_{DIC}$ did not decrease relative to the surface ocean and $\Delta^{14}C$ was only ~50‰ lower during the late glacial. Model simulations of the hypothesized ventilation change during deglaciation lead to large increases in $\delta^{13}C_{DIC}$, $\Delta^{14}C$ and $\varepsilon^{14}C$ that are not recorded in observations.

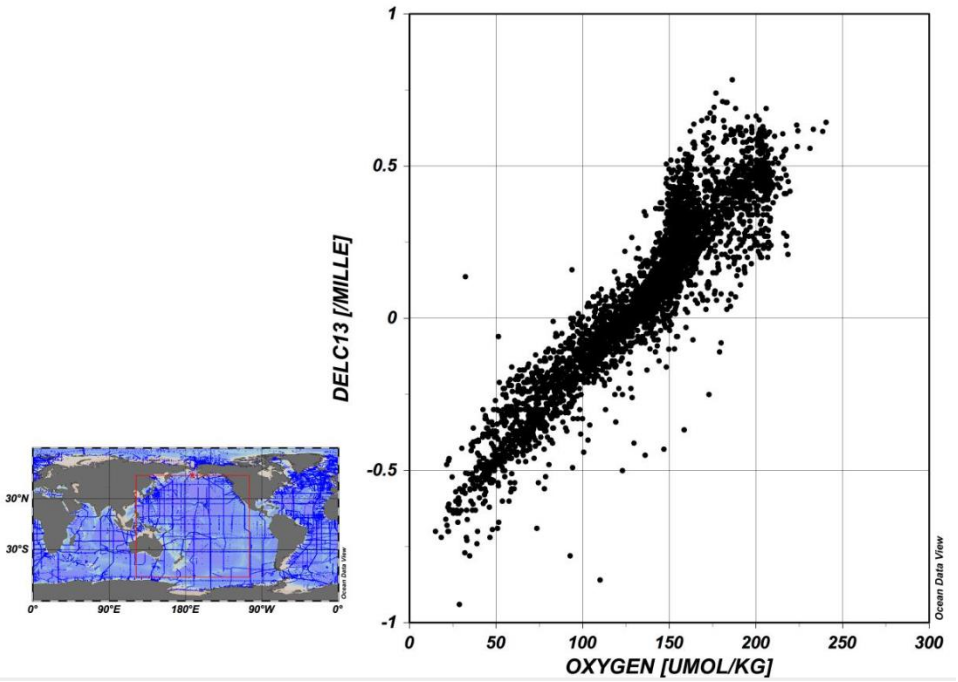

Figure 1. Plot of $\delta^{13}C$ of DIC vs dissolved $O_2$from the GLODAP database of sites in the Pacific

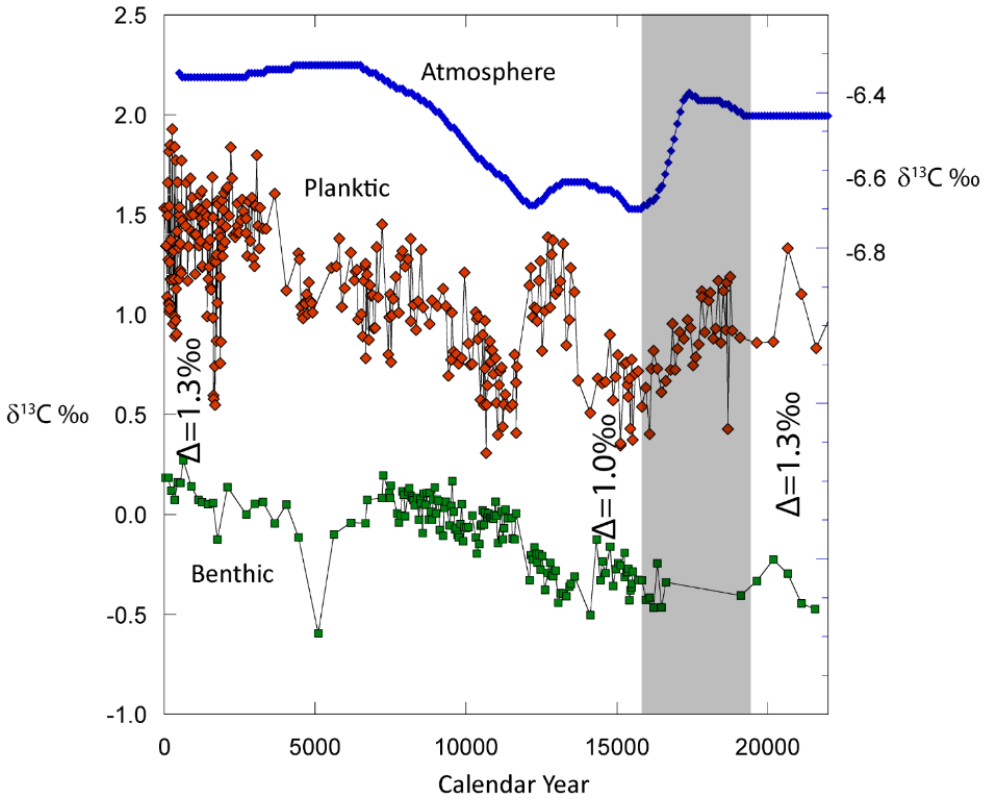

Figure 2. The record of atmospheric $\delta^{13}C$ (CO_2) (Schmitt et al., 2012), planktic (G. ruber) $\delta^{13}C$ and benthic (C.mundulus) $\delta^{13}C$ from core MD98-2181 from the western tropical Pacific. All values are plotted relative to the VPDB standard. Located at 2114m water depth, the core is bathed today by Pacific Deep Water.

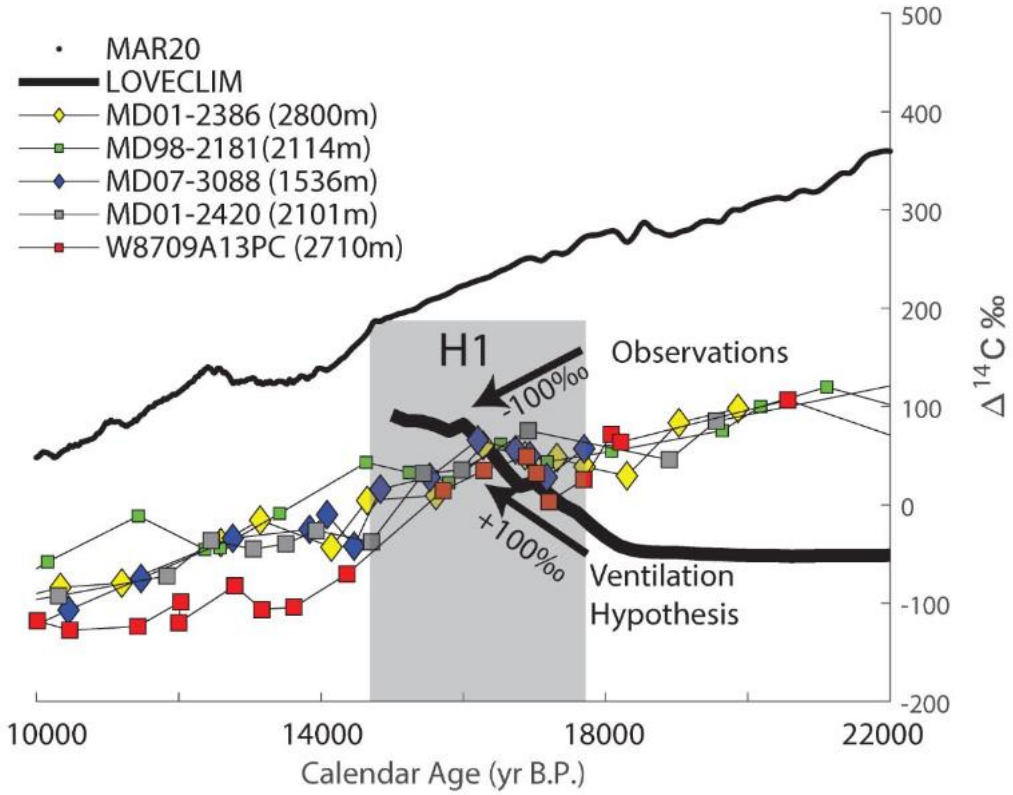

Figure 3. Lower Panel Benthic $\Delta^{14}C$ from the deep Pacific cores. Lower Panel, MARINE20 (global surface ocean) $\Delta^{14}C$ (Heaton et al., 2020). The solid black line is the simulated deep Pacific (130E-130W, 0-50N, 2000-3000m) $\Delta^{14}C$ response to enhanced ventilation during the deglaciation using LOVCLIM (Menviel et al., 2018). Core MD98-2181 data is from this study. Raw 14C ages from Core MD01-2386 (Broecker et al., 2008); MD07-3088 (Siani et al., 2013); MD01-2420 (Okazaki, 2012); W8709A-13PC (Lund, 2013).

3. 古造山带中长期的海山俯冲作用:来自古生代南天山的证据

翻译人：冯婉仪 fengwy@sustech.edu.cn

Wan B, Wang X S, Liu X J. et al. ***Long-lived seamount subduction in ancient orogens: Evidence from the Paleozoic South Tianshan*** *[J]. Geology, 2021, online.*

https://doi.org/10.1130/G48547.1

摘要：在当今环太平洋俯冲带中，海山俯冲对地震活动和弧岩浆作用等俯冲动力学有着显著的影响。由于海山俯冲在地球历史的大部分时间里都发生过，它对上覆板块造山作用的影响应该可以在古造山带中识别出来。本文对中亚古生代南天山造山带进行了研究，发现了大量的海山俯冲证据，并进一步证实了在随后增生的塔里木克拉通上存在着一个由长期存在的地幔柱导致的大火成岩省。研究发现，大约 400-330 Ma 的半连续海山俯冲使弧岩浆活动暂时停止，一旦海山完全俯冲，弧岩浆活动又恢复，榴辉岩也迅速被剥露出来。如果可以在古代造山带中识别出这样一个海山俯冲的造山标记，我们可以恢复更完整的地幔柱俯冲作用及其对地壳和地幔过程的影响。

ABSTRACT: Along the present-day circum-Pacific subduction girdle, seamount subduction is known to have significant effects on subduction dynamics including on seismicity and arc magmatism. Because seamount subduction should have occurred throughout much of Earth history, its effects on orogenesis in the overriding plate should be identifiable in ancient orogens. In this study, we investigate the Paleozoic South Tianshan orogen of Central Asia, for which abundant evidence of seamount subduction exists, further bolstered by the continuation of a long-lived plume-induced large igneous province on the subsequently accreted Tarim craton. We find that semi-continuous seamount subduction from ca. 400 to 330 Ma temporarily shut down arc magmatism, and once the seamounts were completely subducted, then arc magmatism resumed and eclogites were quickly exhumed. If such an orogenic fingerprint of seamount subduction can be identified in ancient orogens, a much more complete picture of plumesubduction interaction and its influence on both crustal and mantle processes can be developed.

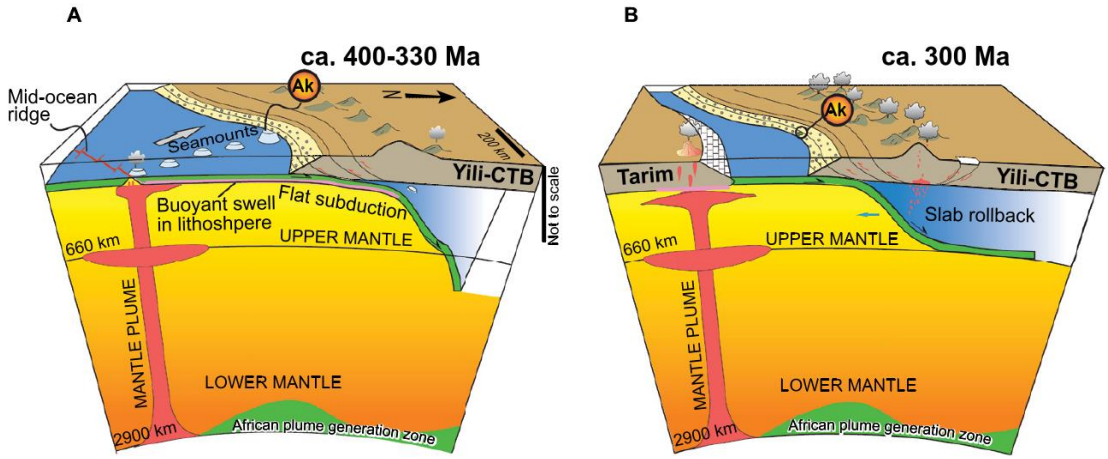

Figure 1. Illustration of the relationship between a long-lived stationary plume and plate motion. (A) Seamount formation and subduction. Subducting slab on which seamounts are located undergoes flat-slab subduction, and no arc magmatism occurs above the seamount region. (B) Tarim large igneous province following seamount subduction. Oceanic slab without seamounts has experienced slab rollback, eclogite exhumation, and widespread arc magmatism. African plume generation zone is from Torsvik et al. (2014). Ak—Akeyazi (China); CTB—Central Tianshan block.

4. Shatsky Rise 的磁异常图及其对海底高原形成的影响

翻译人：李园洁 liyj3@sustech.edu.cn

Huang, Y., Sager, W. W., Zhang, J., Tominaga, M., Greene, J., & Nakanishi, M. ***Magnetic anomaly map of Shatsky Rise and its implications for oceanic plateau formation[J]. Journal of Geophysical Research: Solid Earth****, 2020. 125, e2019JB019116.*

https://doi.org/10.1029/2019jb019116

摘要：Shatsky Rise 海底高原在地磁极性发生快速倒转的时期形成，因而可以利用海洋磁异常重建其构造过程。之前的研究主要集中在识别磁异常等时线，但在高地上追踪磁异常条带存在困难。本文综合大量的 Shatsky Rise 及周围的磁异常数据，包括过去 54 年 96 条航次的 5.5×106 个数据点。时间跨度大和数据集分布不均匀使得融合数据存在挑战。处理过程中去掉内部场，外部场和奇异点。利用最近的以 GPS 导航数据为基础的“backbone”方法来提高数据集的一致性。新磁异常图的显著特征是普遍存在的条带状磁异常。在数据密集的地区可以勾勒出异常的走向，海底高原和周围的洋壳主要特征是条带状磁异常。在一些区域的间断的磁异常指示了与三联点和洋脊重整相关的复杂构造。Tamu Massif 沿着太平洋-法拉隆扩张脊的一段形成，在三联点经过此处时，扩张脊旋转了 90° 。Ori Massif 在三联点之间的太平洋-伊邪那岐脊上形成。Shirshov Massif 包含间断的线性异常，指示着微板块。Shatsky Rise 中的条带状磁异常广泛出现表明这些火山机构形成于类似形成异常厚洋壳的大洋中脊的扩张而产生的。

ABSTRACT：Shatsky Rise oceanic plateau was emplaced during a period of frequent geomagnetic polarity reversals, allowing reconstruction of its tectonic evolution using magnetic anomalies. Prior studies mainly focused on identifying magnetic isochrons and encountered difficulties in tracing magnetic lineations over high relief. We complied a large magnetic data set over Shatsky Rise and its environs, using 5.5×106 data points from 96 geophysical cruises spanning 54 years. The long-time span and heterogeneity of component data sets made data merge a challenge. Contributions of internal and external fields, and spurious readings were removed during processing. A “backbone” method, using recent GPS-navigated data as a foundation, was developed to improve the coherency of the data set. The singular characteristic of the new magnetic anomaly map is that linear magnetic

anomalies are ubiquitous. In nearly every place where data are dense enough to delineate anomaly trends, the plateau and surrounding crust are characterized by linear anomalies. Discordant anomalies in some areas imply complex tectonics related to triple junction migration and ridge reorientation. Tamu Massif apparently formed along a segment of Pacific-Farallon spreading ridge that rotated by 90° as a triple junction migrated through the edifice. Ori Massif appears to have formed on the Pacific-Izanagi ridge between triple junctions. Shirshov Massif contains discordant lineations that may indicate a microplate. The pervasive occurrence of linear magnetic anomalies within Shatsky Rise implies that these volcanic edifices must have formed by spreading analogous to mid-ocean ridges that formed anomalously thick crust.

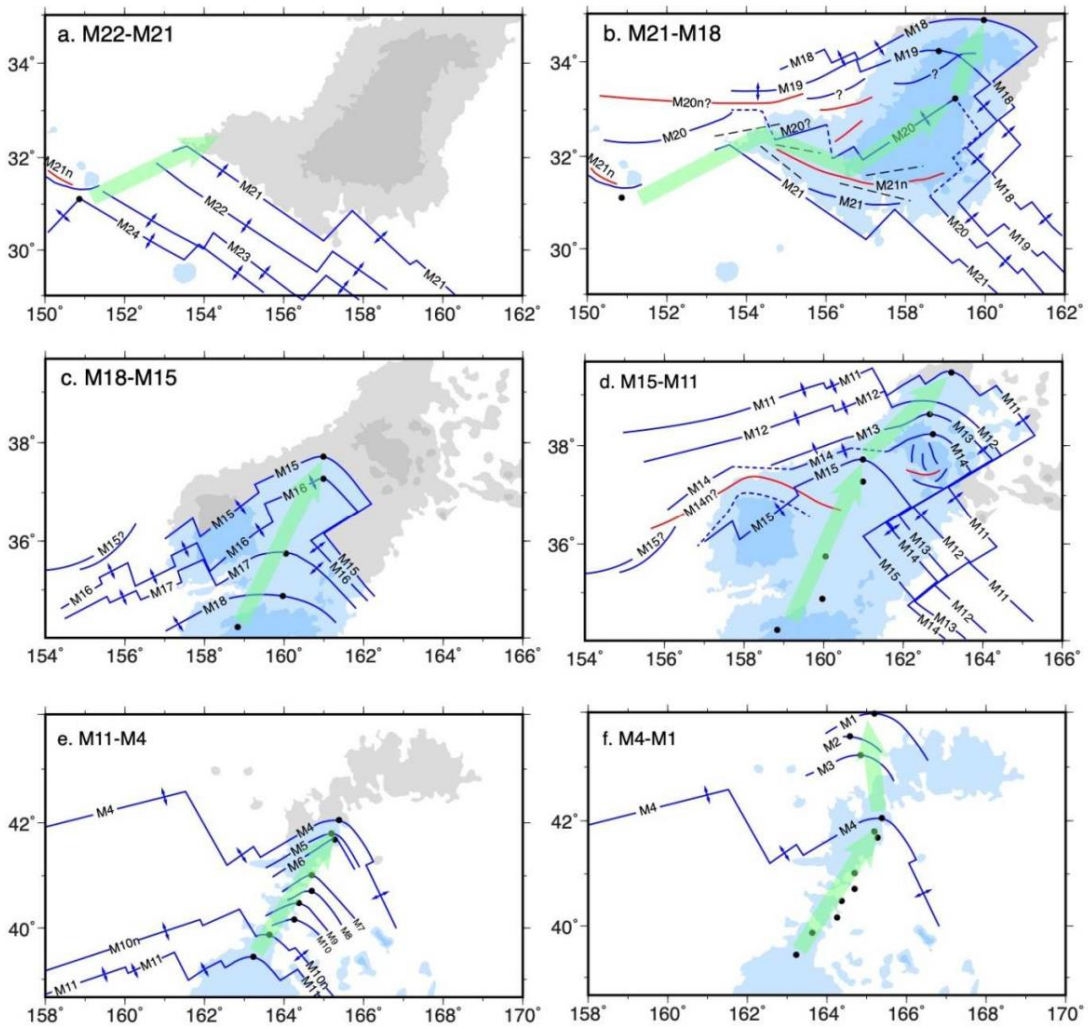

Figure 1. Evolution of spreading ridges and triple junction(s) during the formation of Shatsky Rise. Plots show magnetic anomalies recorded by the Pacific plate. Six intervals are shown: (a) M22-M21, (b)M21-M18, (c) M18-M15, (d) M15-M11, (e) M11-M4, (f) M4-M1. Blue (red) lines denote negative (positive)

magnetization isochrons (negative isochrons are caused by normal polarity magnetization). Double-ended arrows represent spreading directions. Black dots show the location of the Pacific-Farallon-Izanagi triple junction and green arrows show migration of the P-F-I triple junction. Black dashed lines denote V-shaped anomaly features probably caused by propagating ridges.

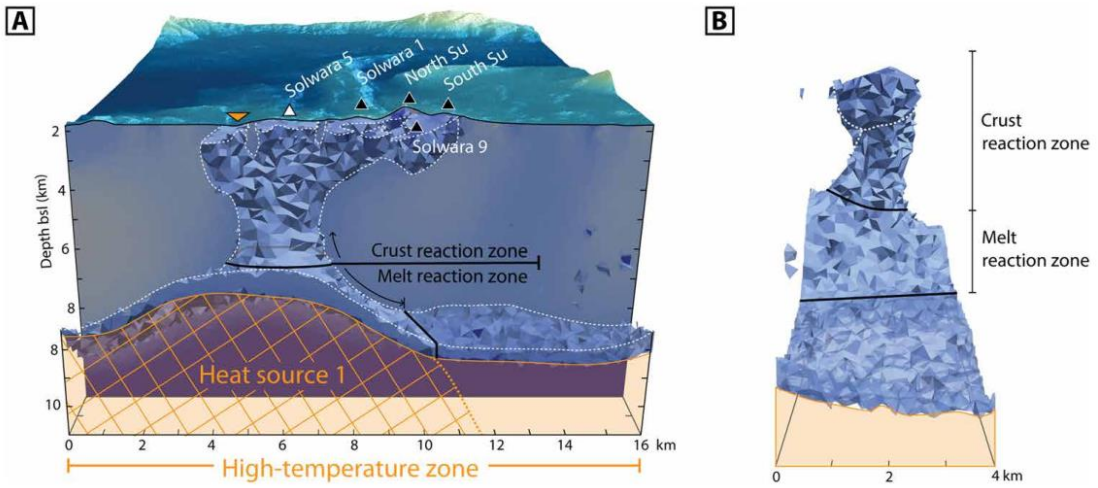

Figure 3. A 3D model of the high-temperature hydrothermal upflow column below the Tumai Ridge. The shown cross section is B-B′ from Fig. 2, with the alteration column visualized with a 0.12 SI threshold of the regional model’s effective magnetic susceptibility. (A) View of the column facing northeast. (B) View of the same column facing northwest. All surface hydrothermal feature symbols and the color scale follow the legend in Fig. 2.

5. 黑海地区大气环流对格陵兰间冰段 GI-10 的滞后响应

翻译人：柳加波 Liujb@sustech.edu.cn

Czymzik M, Nowaczyk N R, Dellwig O, et al. ***Lagged atmospheric circulation response in the Black Sea region to Greenland Interstadial 10****[J]. Proceedings of the National Academy of Sciences, 2020, 117(46): 28649-28654.*

https://doi.org/10.1073/pnas.2005520117

摘要：在末次冰期，北半球高纬气候变化被认为以复杂的方式在影响全球。研究这些变化的演变需要对所选择的环境档案进行精确年代同步。将宇宙成因的放射性核素 ^{10}Be 的全球一致生产率变化在不同档案库中进行比对，可为此类年代同步提供一种方法。本文，我们报道了一个分辨率高于 40 年的 ^{10}Be 记录以及十年尺度的黑海沉积物代用记录。这两个记录包含了格陵兰间冰段（GI-10），约∽41 ka BP 左右的 Laschamp 地磁漂移事件。根据全球范围内一致的生产率变化，我们将 ^{10}Be 记录与格陵兰冰芯的记录进行了年代同步。年代同步后的环境指标显示，在 GI-10 开始时，黑海地区出现了二分的气候响应。首先，与格陵兰岛变暖相伴的是，黑海中沉积的冰筏碎屑含量减少，表明冬季不那么严峻。其次，伴随着 190（±44）年的滞后，陆源 K / Ti 比和自生 Ca 沉淀的增加表明区域降水增加和湖面温度升高。我们通过大气循环的主导模式的变化来解释这种滞后的气候响应，这可能与区域热海洋内部对间冰段气候的穿时(time-transgressive)调整有关。

ABSTRACT: Northern Hemispheric high-latitude climate variations during the last glacial are expected to propagate globally in a complex way. Investigating the evolution of these variations requires a precise synchronization of the considered environmental archives. Aligning the globally common production rate variations of the cosmogenic radionuclide 10Be in different archives provides a tool for such synchronizations. Here, we present a 10Be record at <40-y resolution along with subdecadal proxy records from one Black Sea sediment core around Greenland Interstadial 10 (GI-10) ~41 ka BP and the Laschamp geomagnetic excursion. We synchronized our 10Be record to that from Greenland ice cores based on its globally common production rate variations. The synchronized environmental proxy records reveal a bipartite climate response in the Black Sea

region at the onset of GI-10. First, in phase with Greenland warming, reduced sedimentary coastal ice rafted detritus contents indicate less severe winters. Second, and with a lag of 190 (± 44) y, an increase in the detrital K/Ti ratio and authigenic Ca precipitation point to enhanced regional precipitation and warmer lake surface temperatures. We explain the lagged climatic response by a shift in the dominant mode of atmospheric circulation, likely connected with a time-transgressive adjustment of the regional thermal ocean interior to interstadial conditions.

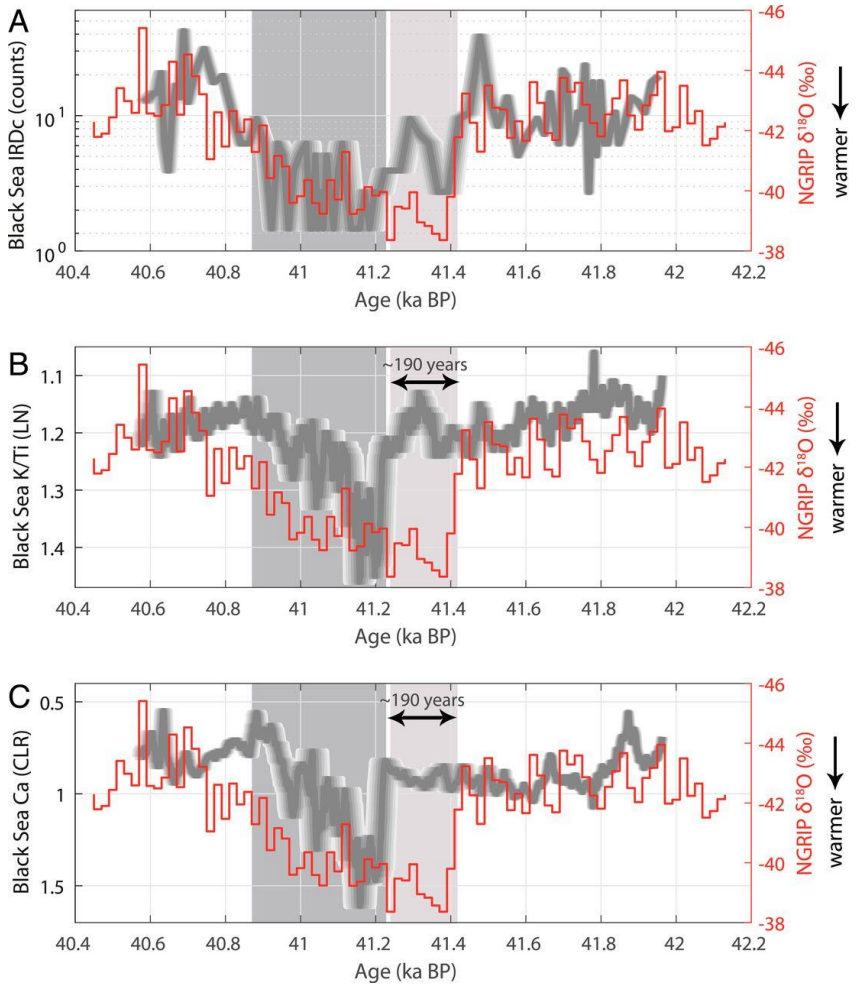

Figure 1. Synchronized paleoclimate records from Black Sea sediment core M72/5-22GC8 and the Greenland NGRIP ice core around GI-10. (A) Black Sea IRDc and NGRIP δ18O. (B) Black Sea K/Ti ratio (reversed axis) and NGRIP δ18O. (C) Black Sea Ca (reversed axis) and NGRIP δ18O. The horizontal spread of the gray Black Sea graphs depicts synchronization uncertainties.

6. 252 Ma 西伯利亚煤炭燃烧破坏全球碳平衡

翻译人：周洋 zhouy3@sustech.edu.cn

Elkins-Tanton L T, Grasby S E, Black B A, et al. ***Field evidence for coal combustion links the 252 Ma Siberian Traps with global carbon disruption*** *[J]. Geology, 2020, v. 48, p. 986–991.*

https://doi.org/10.1130/G47365.1

摘要：二叠-三叠纪的生物大灭绝是地球历史上最严重的灭绝事件。西伯利亚火山喷发可能影响了全球的大气变化，导致生物灭绝。在地球年代学的不确定性范围内，一个明显的负碳同位素事件恰好与西伯利亚溢流玄武岩 Norilsk 部分的最老的岩石相吻合。 我们集中研究了西伯利亚大量的火山碎屑岩，这些岩层为含碳气体的潜在载体。在过去 6 年的野外工作中，我们收集了整个西伯利亚地台的岩石样品，在这里显示的第一个直接证据表明西伯利亚南部最早的火山喷发燃烧了大量的植被和煤炭。我们认为有机物的量和组成与岩浆作用密切相关，引起全球碳同位素变化，可能极大地促进了生物的灭绝。。

ABSTRACT: The Permian-Triassic extinction was the most severe in Earth history. The Siberian Traps eruptions are strongly implicated in the global atmospheric changes that likely drove the extinction. A sharp negative carbon isotope excursion coincides within geochronological uncertainty with the oldest dated rocks from the Norilsk section of the Siberian flood basalts. We focused on the voluminous volcaniclastic rocks of the Siberian Traps, relatively unstudied as potential carriers of carbon-bearing gases. Over six feld seasons we collected rocks from across the Siberian platform, and we show here the frst direct evidence that the earliest eruptions in the southern part of the province burned large volumes of a combination of vegetation and coal. We demonstrate that the volume and composition of organic matter interacting with magmas may explain the global carbon isotope signal and may have signifcantly driven the extinction.

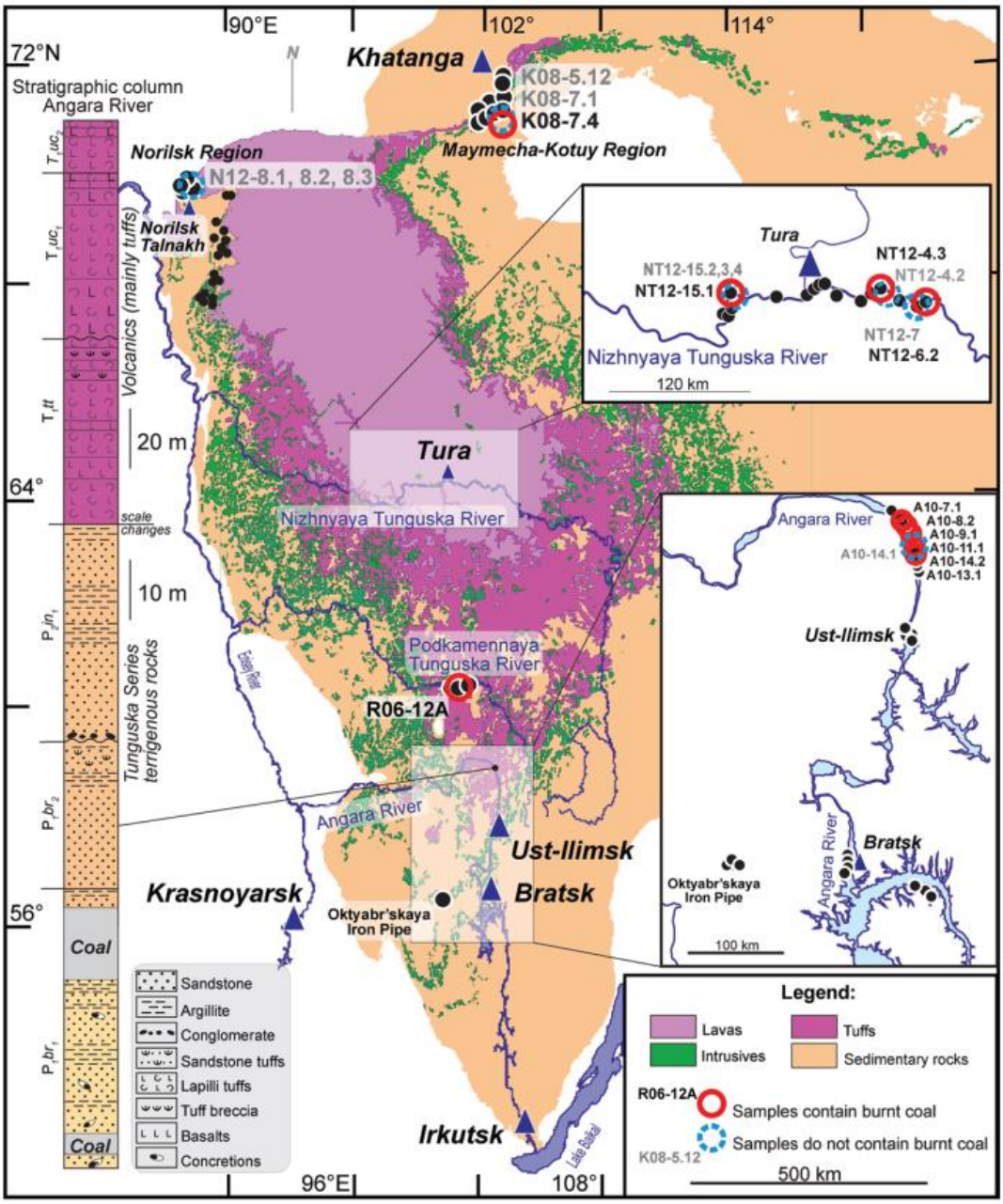

Figure 1. Map showing early southern volcaniclastics of the Siberian Traps that display abundant evidence for coal burning. Black dots mark sampling areas from the larger Siberian flood basalts and end-Permian extinction research project (funded under U.S. National Science Foundation grant EAR-0807585). Samples analyzed but with no coal found are labeled in gray with blue circles; those with red circles and black labels contain combusted, coked, or thermally altered coal. The majority of southern volcaniclastics analyzed contain coal, but only one from the northern Kotuy and Norilsk regions; in the intermediate Nizhnyaya Tunguska region, three out of eight samples contained coal. Map after Svensen et al. (2009) and Malich et al.(1974); stratigraphic column after Permyakov et al. (2012). On the stratigraphic column: P1br1 and P1br2—lower and upper parts of the Burguklinskaya Formation (Lower Permian), respectively; P2in1—lower part of the Inganbinskaya Formation (Middle Permian); T1tt—Tutonchanskaya Formation (Lower Triassic); T1uc1 and T1uc2—lower and upper parts of the the Uchamskaya Formation (Lower Triassic), respectively.

7. 南海新生代裂谷盆地结构与运动学综合分析

翻译人：刘伟 inewway@163.com

Wang P, Li S, Suo Y, et al. ***Structural and kinematic analysis of Cenozoic rift basins in South China Sea: A synthesis****[J].* ***Earth-Science Reviews****, 103522.*

https://doi.org/10.1016/j.earscirev.2021.103522

摘要：东亚大陆边缘东近太平洋板块俯冲域，西连印-欧亚碰撞域。这两个动力域的时空相互作用产生了右旋走滑-伸展应力场，导致新生代地球上近 75%的边缘海和大陆边缘裂谷形成。其中，南海及其北缘位于太平洋构造域和特提斯构造域的核心。南海及其北缘表现为显著的磁异常条带和强烈的裂谷作用，对南海及其北缘的演化具有重要意义。尽管对新生代边缘海和裂谷盆地进行了很多研究，但对它们的形成机制仍不明确。本文通过对南海北缘地震剖面和断裂构造资料的综合分析，来探究南海北缘新生代构造演化。在详细的几何和运动学结构分析的基础上，我们论证了北东向和北东东向走滑断层在平面上组装成马尾状或羽状构造，在地震剖面上表现为花状构造。在南海北缘发现了两期北东向断裂。古新世—中始新世早期(~44- 42 Ma)发育早期斜向伸展，并伴有强烈的裂谷作用和一些左阶雁列式断裂体系。中始新世晚期至中新世早期(~21 Ma)发育右旋右阶张扭性断裂体系。西边的印度-欧亚板块碰撞域，东边的太平洋板块俯冲域，南边的古南海板块拉张拖曳体系的共同作用，形成了这两期断裂。我们的研究为控制南海打开的动力学和构造学提供了重要的见解。晚始新世至渐新世，晚期的张扭断裂和右旋走滑断裂体系导致了西北次盆地、东部次盆地和东北次盆地的打开。早中新世，哀老山-红河剪切带的左旋走滑作用和古南海的拉张拖曳作用导致了西南次盆地的打开和东部次盆地扩张方向的改变。

ABSTRACT: The East Asian continental margin straddles the boundary between the Pacific Plate subduction Domain to the east and the Indo-Eurasian collision Domain to the west. The spatial and temporal interaction between these two dynamic domains induced dextral trans-tensional stress field, which resulted in generating nearly 75% of the globe's marginal seas and continental margin rifts during the Cenozoic. Among these, the South China Sea (SCS) and its northern margin are located in the core of the Pacific Tectonic Domain and the Tethyan Tectonic Domain. The evolution of the

SCS and its northern margin are of prime interest because of the spectacular magnetic lineation and strong rifting. In spite of the several investigations on the Cenozoic marginal seas and rift basins occurred, their mechanisms of formation remain equivocal. Here we perform a comprehensive analysis of seismic profiles and fault architecture data with a view to understanding the Cenozoic tectonic evolution of the northern margin of the SCS. Based on detailed structural analysis of the geometry and kinematics, we demonstrate that the NE- and ENE-striking faults assembled to horsetail- or feather-shaped structures in plan view, with flower-like structures on seismic profiles. Two stages of faulting with NE-trending are identified along the northern margin of the SCS. The earlier oblique extension developed during the Paleocene to the early Middle Eocene (~44–42 Ma), accompanied by strong rifting and some left-stepping en echelon-like faults. The later trans-tensional faulting developed during the late Middle Eocene to the Early Miocene (~21 Ma), resulting in the formation of the dextral right-stepping trans-tensional fault system. Two stages of faulting were linked to the joint effect among the collision domain of Indian-Eurasian plates to the west, the subduction domain of the Pacific Plate to the east and the slab-pull system of the proto-SCS to the south. Our study provides important insights into the dynamics and tectonics that controlled the opening of the South China Sea. During the Late Eocene to the Oligocene, the later trans-extensional faulting and right-stepping strike-slip fault system caused the opening of the Northwest Sub-basin, East Sub-basin and Northeast Sub-basin. However, during the Early Miocene, the left-lateral strike-slip of the Ailao Shan-Red River (ASRR) shear zone and the slab-pull force of the Proto-SCS resulted in the opening of the Southwest Sub-basin and the change in the spreading direction of the East Sub-basin.

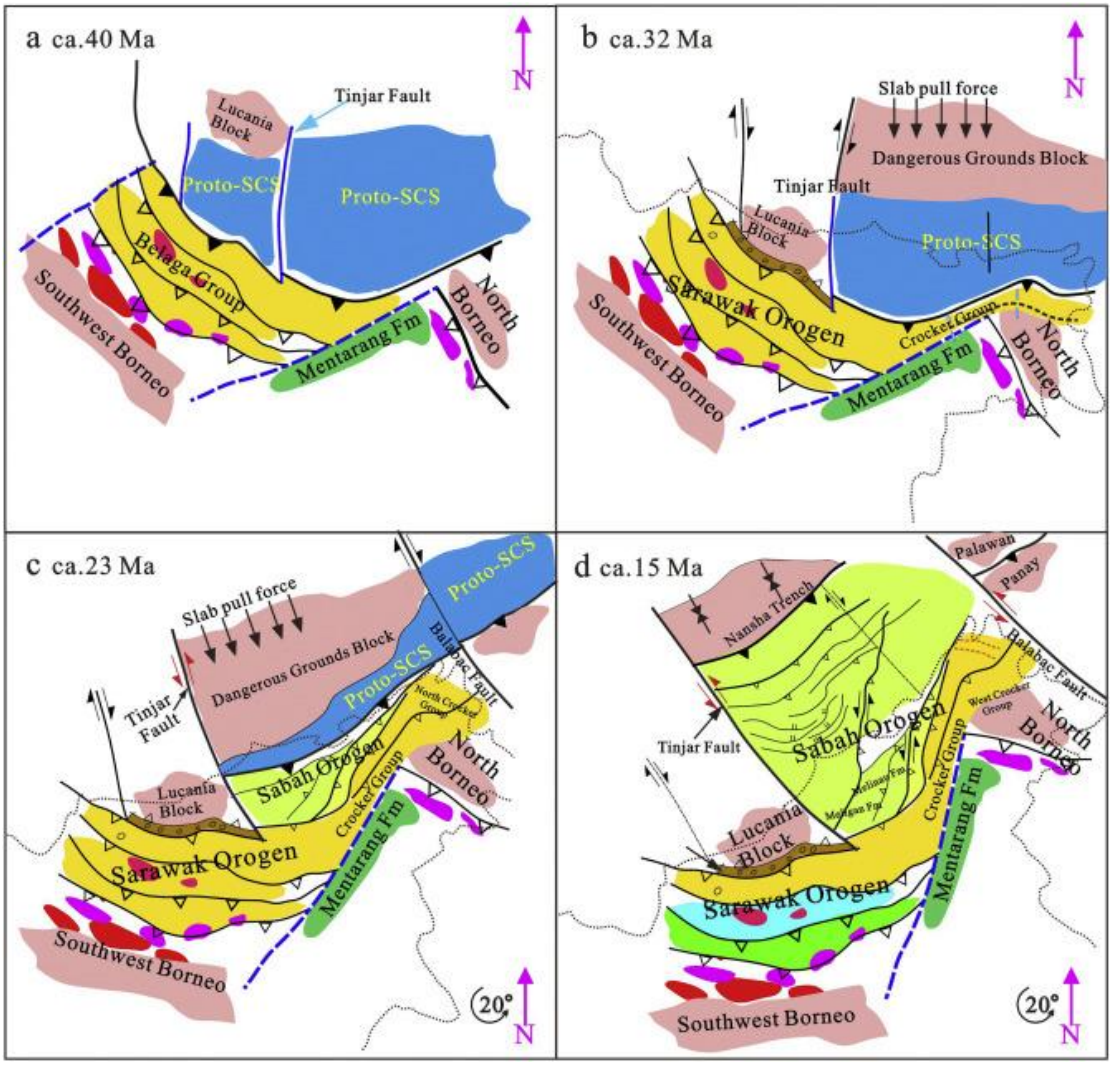

Figure 1. The tectonic evolution model of SCS.

8. 中国北部和蒙古南部的冬季积雪如何连接东亚冬季风和夏季风

翻译人：杨会会 11849590@mail.sustech.edu.cn

Lu M M, Kuang Z M, Yang S and et al. ***A Bridging Role of Winter Snow over Northern China and Southern Mongolia in Linking the East Asian Winter and Summer Monsoons[J].Journal of climate****, 10.1175/JCLI-D-20-0298.1.*

https://doi.org/10.1175/JCLI-D-20-0298.1.

摘要：欧亚地区的雪是影响亚洲季风的最重要因素之一，长期以来一直被认为是季风的预测器。 本研究根据观测和模型模拟证明了中国北部和蒙古南部（NCSM）的积雪异常，对东亚冬季风和东亚夏季风的桥梁作用。NCSM 的积雪增加导致地表和对流层冷却，进而北风异常导致冷空气入侵增强，最终导致了东亚冬季风的增强。反过来，更强的冬季风为东亚往南的降雪增强提供了条件，导致了“降雪增强-东亚冬季风增强”的交互作用。由于融雪和湿润水汽的记忆效应以及春天“降雪-季风”的交互作用，陆地冷却会一直持续到夏天。这就导致了夏季经向温度梯度及其有关的上层西风带的变化。青藏高原北部增强的西风带与高原的地形相互作用导致下游异常的辐合和向南的补偿性辐散。所以，中国东北部和朝鲜半岛上方出现异常的气旋环流和降雨增加，但是在副热带东亚-太平洋地区出现反气旋环流和降雨减少。而且，有限的分析表明，比起海表温度反馈，降雪异常对“东亚冬季风-东亚夏季风”的直接影响似乎更重要。

ABSTRACT: Eurasian snow, one of the most important factors that influence the Asian monsoons, has long been viewed as a useful predictor for seasonal monsoon prediction. In this study, observations and model simulations are used to demonstrate a bridging role of the winter snow anomaly over northern China and southern Mongolia (NCSM) in the relationship between the East Asian winter monsoon (EAWM) and the East Asian summer monsoon (EASM). Enhanced snow in NCSM results in local surface and tropospheric cooling, strengthening the EAWM through cold air intrusion induced by northerly wind anomalies. In turn, the stronger EAWM provides a favorable condition for enhanced snowfall over East Asia to the south, indicating an active snow-EAWM interaction. The continental cooling could be maintained until summer due to the memory effect of snowmelt and moistening as well as the snow-monsoon interaction in the spring, causing changes

in the meridional temperature gradient and associated upper-level westerlies in the summer. The interaction between the strengthened westerlies over the northern Tibetan Plateau and the topography of the plateau could lead to anomalous downstream convergence and compensating divergence to the south. Therefore, anomalous cyclonic circulation and increased rainfall occur over northeastern China and the Korean Peninsula, but anticyclonic circulation and decreased rainfall appear over the subtropical East Asian-Pacific region. Moreover, limited analysis shows that, compared to sea surface temperature feedback, the direct impact of snow anomaly on the EAWM-EASM connection seems more important.

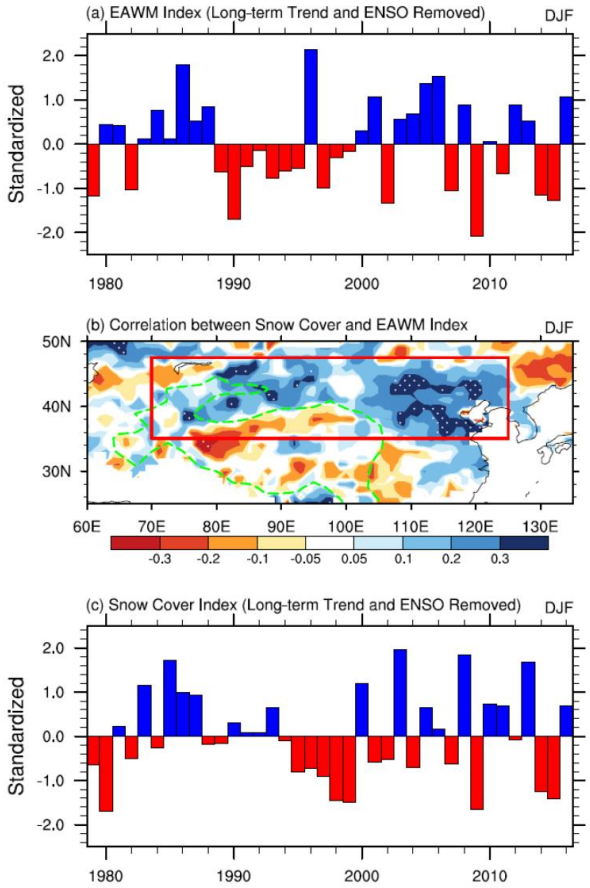

Figure 1. (a) Standardized time series of EAWM index with its linear trend and the linearly regressed signal of ENSO removed. (b) Correlation between winter snow cover and the EAWM index. White dots indicate that the correlation coefficients are above the 90% confidence level. The topography of the Tibetan Plateau above 1500 m is marked with the dashed green contour. The red box indicates the location of snow cover anomaly most strongly associated with the winter monsoon. (c) Standardized time series of snow cover index related to EAWM variability, with its linear trend and the linearly

regressed signal of ENSO removed.

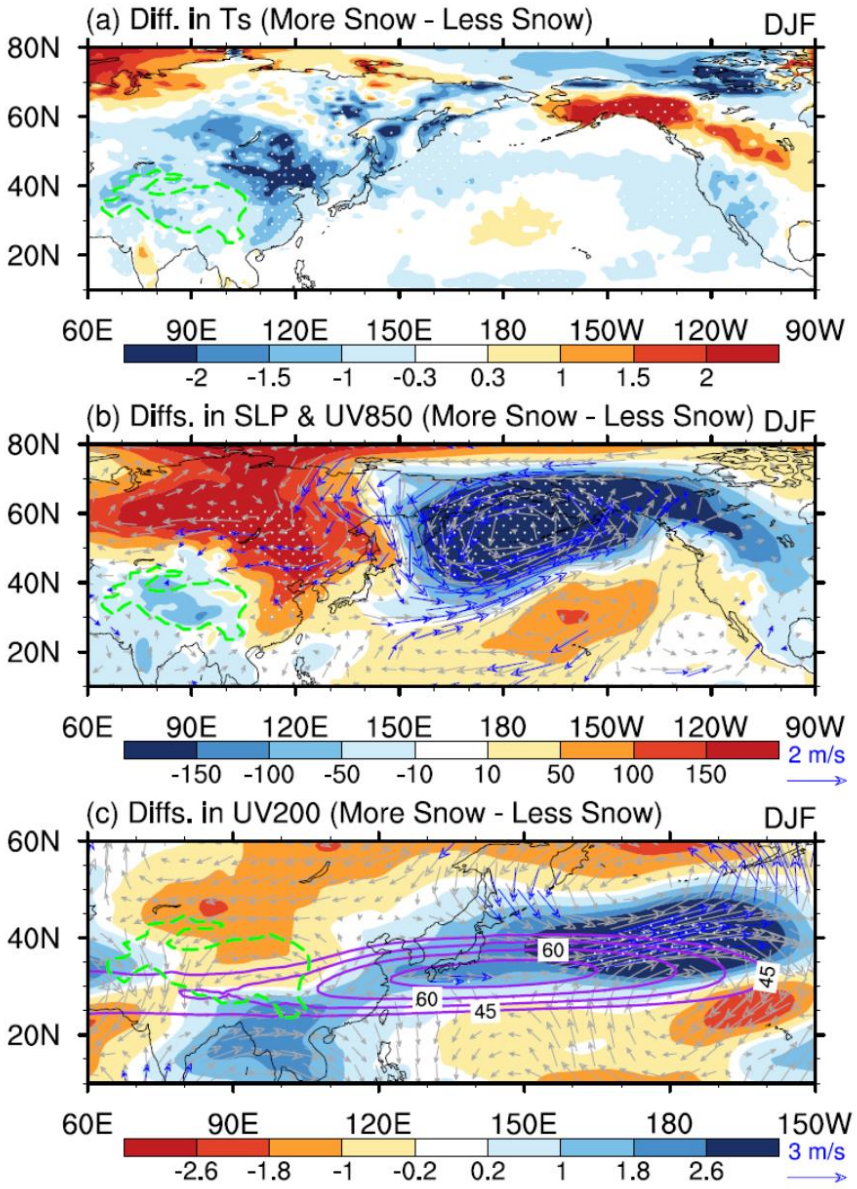

Figure 2. Composite differences in winter (a) surface temperature (shadings, units: °C), (b) sea level pressure (shadings, units: Pa) and horizontal wind at 850-hPa (vectors, units: m s−1) , and (c) 200-hPa zonal wind (shadings, units: m s−1) and wind vectors (vectors, unit: m s−1) between more and less snow cover years. White dots and blue vectors indicate the values above the 90% confidence level. Purple contours in (c) show winter climatology of 200-hPa westerlies. The topography of Tibetan Plateau above 1500 m is marked with the dashed green contour.

9. 埃及北部 Marea/Northern Hawwariya:非侵入性探测和挖掘结果

翻译人：曹伟 11930854@QQ.com

Derda T, Gwiazda M, Misiewicz K, Malkowski W. ***Marea/Northern Hawwariya in northern Egypt: Integrated results of non-invasive and excavation works.*** *[J]* ***Archaeological Prospection.*** *2020.*

https://doi.org/10.1002/arp.1801

摘要：Hawwariya Marea/Northern Hawwariya 是埃及北部 Lake Mareotis 区域最大和最重要的考古遗址之一，可追溯至公元前 3 世纪至公元 8 世纪。虽然挖掘工作从 20 世纪 70 年代末就开始了，但该定居点很大程度上仍未被勘探。为了更深入的了解这一区域，本研究利用精确定位系统和磁强计测量，对该区域 21.5 公顷的土地进行了非侵入性研究。根据获得的数据绘制了精确的地形图和地磁图。同时，还进行了核查研究，包括考古发掘、地表勘察记录以及卫星图像分析。在测量现场的东南部，同步进行了电阻率测量，这种方法可以对拜占庭和早期伊斯兰城镇等密集建筑区域进行识别。在西南侧，测量记录到一些磁异常，呈规则的线性条带状分布，测区周边是湿地，没有明显的居住迹象。在北部，定居点区域被人工海岸线限制，形成了由石块构成的笔直滨水区。在小镇的分布区域，研究发现了一条 260 米长的街道，附近存在正常的建筑群。这种规律性分布表明了规划的有序性，至少对于拜占庭式的定居点来说是存在这种特征。大幅度磁异常的记录证明存在明显火烧的痕迹，它们可能被解释为窑炉的遗迹，也可能是被用来制造双耳陶罐、玻璃器皿和石灰。现场东南部的电阻率测量结果表明，天然石灰岩隆起处存在空洞，这些可能是岩石雕刻的坟墓。对于 Marea /Northern Hawwariya 进行的多学科、非侵入性研究有助于迅速形成关于该遗址空间分布的新了解，极大地丰富了关于其形态和各部分功能的信息。

ABSTRACT: Marea/Northern Hawwariya is one of the largest and most important archaeological sites dating between the 3rd century BC and the 8th century AD located at Lake Mareotis in northern Egypt. Even though excavations have been carried out since the end of the 1970s, the settlement is still largely unexplored. To rectify this situation, non-invasive research has been carried out on 21.5 ha of the site using a precise positioning system and magnetometer measurements. Exact topographic and magnetic maps were prepared based on the data that were obtained.

Simultaneously, verification research were carried out, including archaeological excavations, registering surface findings and satellite image analysis. In the southeastern part of the site, electrical resistivity measurements were taken as well. This approach allowed for the identification of the densely built areas of the Byzantine and Early Islamic town. On the south-western side, some magnetic anomalies were registered, following regular patterns with clear linear borders and surrounded by wetlands without clear signs of habitation. On the northern side, the settlement was limited by an artificial coastline, forming straight waterfronts made of stone blocks. As for the town itself, a 260-m street with adjacent regular built-up areas was discovered. This regularity points to an order of planning, at least for the Byzantine part of the settlement. Recording of large amplitude magnetic anomalies proves the presence of heavily burnt objects. They may be interpreted as remains of kilns, perhaps used to manufacture amphorae, glass vessels and lime. Electrical resistivity measurements in the south-eastern part of the site localized cavities in the natural limestone rock uplift. These may have been rock-cut tombs. Multidisciplinary, non-invasive research in Marea/Northern Hawwariya allowed for the quick generation of new knowledge on the topography of the site, significantly enriching information on its form and the functions of its various parts.

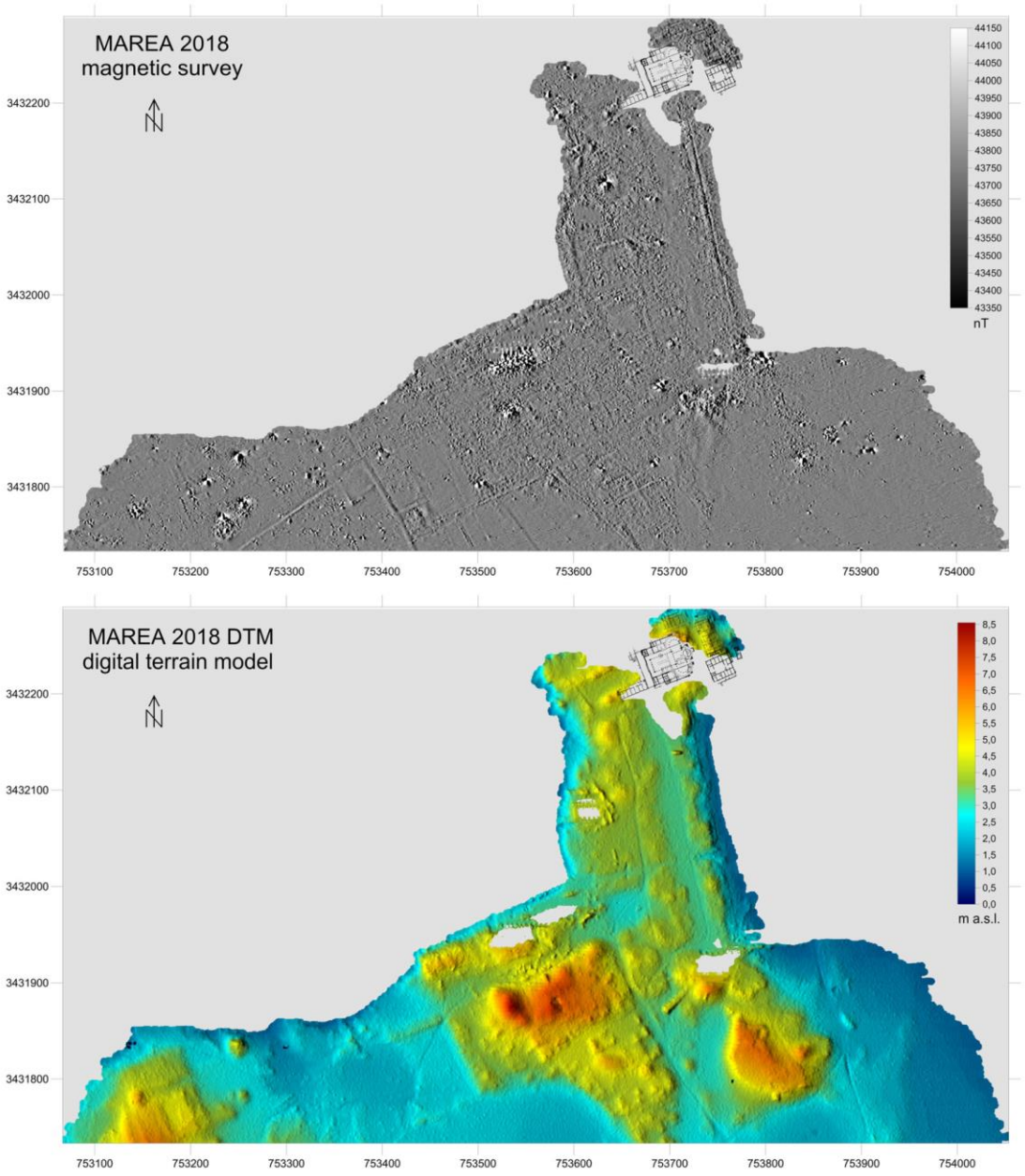

Figure 1. Magnetic survey map (top) and digital terrain model (bottom)

10. 未培养球菌 THC-1 体内非链状排列磁小体生物矿化和磁性特征研究

翻译人：王敦繁 dunfan-W@foxmail.com

Li et al. ***Biomineralization and Magnetism of Uncultured Magnetotactic Coccus Strain THC‐1 With Non‐chained Magnetosomal Magnetite Nanoparticles****[J]. Journal of Geophysical Research: Solid Earth, 2020, 125(12).*

https://doi.org/10.1166/jnn.2007.076

摘要：微生物趋磁细菌(MTB)长期以来一直引起地质学家和生物学家的兴趣，因为它们对磁小体内的细胞内单畴磁铁矿晶体进行生物矿化，这些磁铁矿晶体通常组织成单链或多链。磁化石是一种理想的磁性载体，用于重建古地磁和古环境信息。本文利用透射电子显微镜(TEM)和岩石磁性方法，研究了中国汤河地区未培养的趋磁球菌菌株 THC-1 的磁体磁铁矿的生物矿化和磁性。我们的结果表明，THC-1 产生沿[111]晶体学方向拉长的六方棱柱状磁铁矿单晶。THC-1 中的磁铁矿晶体大部分分散，没有明显的链组装。全细胞 THC-1 样品产生正常的 SD 滞后回线和~112 K 的 Verwey 转变温度。与具有磁小体链(s)的 MTB 细胞相比，THC-1 细胞具有滴状一阶反转曲线分布，表明粒子间存在中度的相互作用。由于磁小体链的缺失，THC-1 的饱和等温剩余磁化率(δFC， δZFC)在场冷和零场冷的 Verwey 转变温度以下和以上的差值(δFC， δZFC)较高， δFC/δZFC 较低。结合之前的研究，我们的结果表明一些 MTB 物种/菌株可以形成没有线性链构型的磁体磁铁矿。MTB 产生的磁铁矿具有不同的磁性能，与其他类型的磁铁矿相比，磁性能是独特的，但不一定是唯一的。因此，将体磁测量与 TEM 观测相结合来识别地质记录中的磁化石仍然是必要的。

ABSTRACT: Microbial Magnetotactic bacteria (MTB) have long fascinated geologists and biologists because they biomineralize intracellular single domain (SD) magnetite crystals within magnetosomes that are generally organized into single or multiple chains. MTB remains in the geological record (magnetofossils) are ideal magnetic carriers and are used to reconstruct paleomagnetic and paleoenvironmental information. Here, we studied the biomineralization and magnetic properties of magnetosomal magnetite produced by uncultured magnetotactic coccus strain THC-1, isolated from the Tanghe River, China, by combining transmission electron microscope (TEM) and rock magnetic approaches. Our results reveal that THC-1 produces

hexagonal prismatic magnetite single crystals that are elongated along the [111] crystallographic direction. Most of the magnetite crystals within THC-1 are dispersed without obvious chain assembly. A whole-cell THC-1 sample yields a normal SD hysteresis loop and a Verwey transition temperature of ~112 K. In contrast to MTB cells with magnetosome chain(s), THC-1 cells have a teardrop first-order reversal curve distribution that is indicative of moderate inter-particle interactions. Due to the absence of a magnetosome chain, THC-1 has relatively high values of the difference between the saturation isothermal remanence magnetization (SIRM) below and above the Verwey transition temperature for field-cooled and zero-field cooled SIRM curves (δFC, δZFC), and a low δFC/δZFC value. Together with previous studies, our results demonstrate that some MTB species/strains can form magnetosomal magnetite without linear chain configurations. Magnetite produced by MTB has diverse magnetic properties, which are distinctive but not necessarily unique compared to other magnetite types. Therefore, combining bulk magnetic measurements and TEM observations remains necessary for identifying magnetofossils in the geological record.

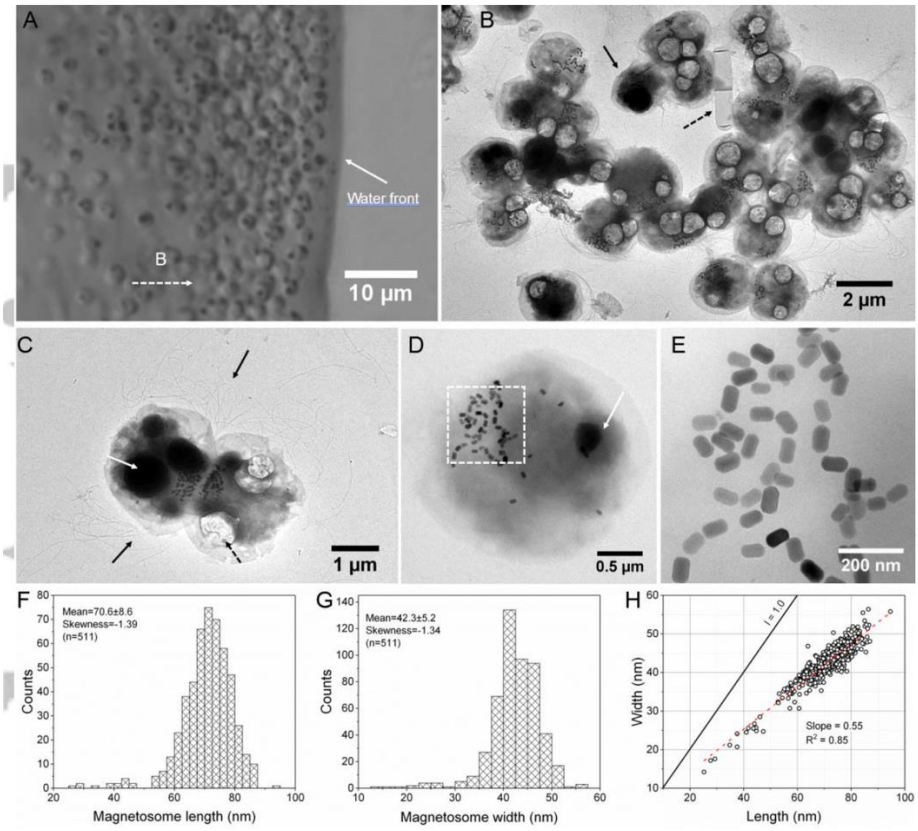

Figure 1. Morphological features of THC-1 cells. (A) Optical microscope image of living THC-1 cells swimming out from a small drop of sediment on the left along an applied magnetic field (B, indicated by the white dashed line with arrow), and accumulating at the water front (indicated by

the white solid line with arrow). (B) Low-magnification TEM image of many THC-1 cells collected from sediments. The black solid line with arrow indicates another MTB type, which contains magnetic particles organized into a single chain. The black dashed line with arrow indicates two non-MTB rod bacteria. (C) TEM image of two THC-1 cells that are dividing. Magnetic particles are roughly evenly distributed between the two daughter cells. Two flagellae bundles on one side of the cell are indicated by a black solid line with arrow. Beside magnetosomes, the left-hand cell contains three electron-condensed globules (black); the right-hand one contains three electron-transparent vacuoles (black dashed line with arrow). (D) TEM image of a THC-1 cell with spherical morphology and an irregular inclusion (white solid line with arrow). (E) Close-up of the area outlined by a white dashed rectangle in (D). Some magnetic particles appear to be organized partially in small chains from two-dimensional TEM observations, but 3D electron tomography analysis indicates they are dispersed (see Fig. 3). (F, G) Histograms of magnetic particle (F) length and (G) width. (H) Plot of crystal length vs. width with a linear relationship.

11. 利用洞穴沉积物钙同位素对加州 8.2kyr 事件期间降水的半定量估算

翻译人：李海 12031330@mail.sustech.edu.cn

de Wet, C. B., Erhardt, A. M., Sharp, W. D., Marks, N. E., Bradbury, H. J., Turchyn, A. V., et al. (2020). ***Semi‐Quantitative Estimates of Rainfall Variability during the 8.2kyr Event in California using Speleothem Calcium Isotope Ratios****[J].* ***Geophysical Research Letters****, 47, e2020GL089154.*

https://doi.org/10.1029/2020GL089154

摘要：石笋的多个参数揭示了8.2kyr事件期间加利福尼亚海岸的水气变化，前兆事件可能是由阿加西兹湖的初始排水引起。我们利用洞穴沉积物的 $\delta^{44}Ca$，并通过对现代气候和洞穴环境的测量结果进行标定，获得了加州地区古降水变化的第一个半定量估计值。我们发现在8.2kyr事件期间降水变化的幅度接近最近（1950-2019）可观测到的多年变化，前兆事件期间的变化幅度可能超过该范围。此外，我们发现存在多个与前兆事件期间变化幅度相当的阶段。我们的研究表明，洞穴沉积物的钙同位素比值是重建古降水的一种强有力的半定量手段，尽管在应用这种方法之前，每个洞穴系统都必须评估许多因素。

ABSTRACT: A multi‐proxy record from a fast‐growing stalagmite reveals variable hydroclimate on the California coast across the 8.2kyr event and a precursor event likely caused by initial drainage of proglacial Lake Agassiz. Using speleothem $\delta^{44}Ca$, we develop the first semi‐quantitative estimates of paleo‐rainfall variability for California through calibration with measurements of the modern climate and cave environment. We find that the magnitude of rainfall variability during the 8.2kyr event approached the multi‐year variability observable in the recent past (1950–2019) and the magnitude of variability during the precursor event likely exceeded this range. Additionally, we observe other instances of multi‐decadal variability comparable in magnitude to the precursor event during the record. Our work suggests that speleothem calcium isotope ratios are a powerful semi‐quantitative means to reconstruct paleo‐rainfall, although numerous factors must be assessed in each cave system before applying this approach.

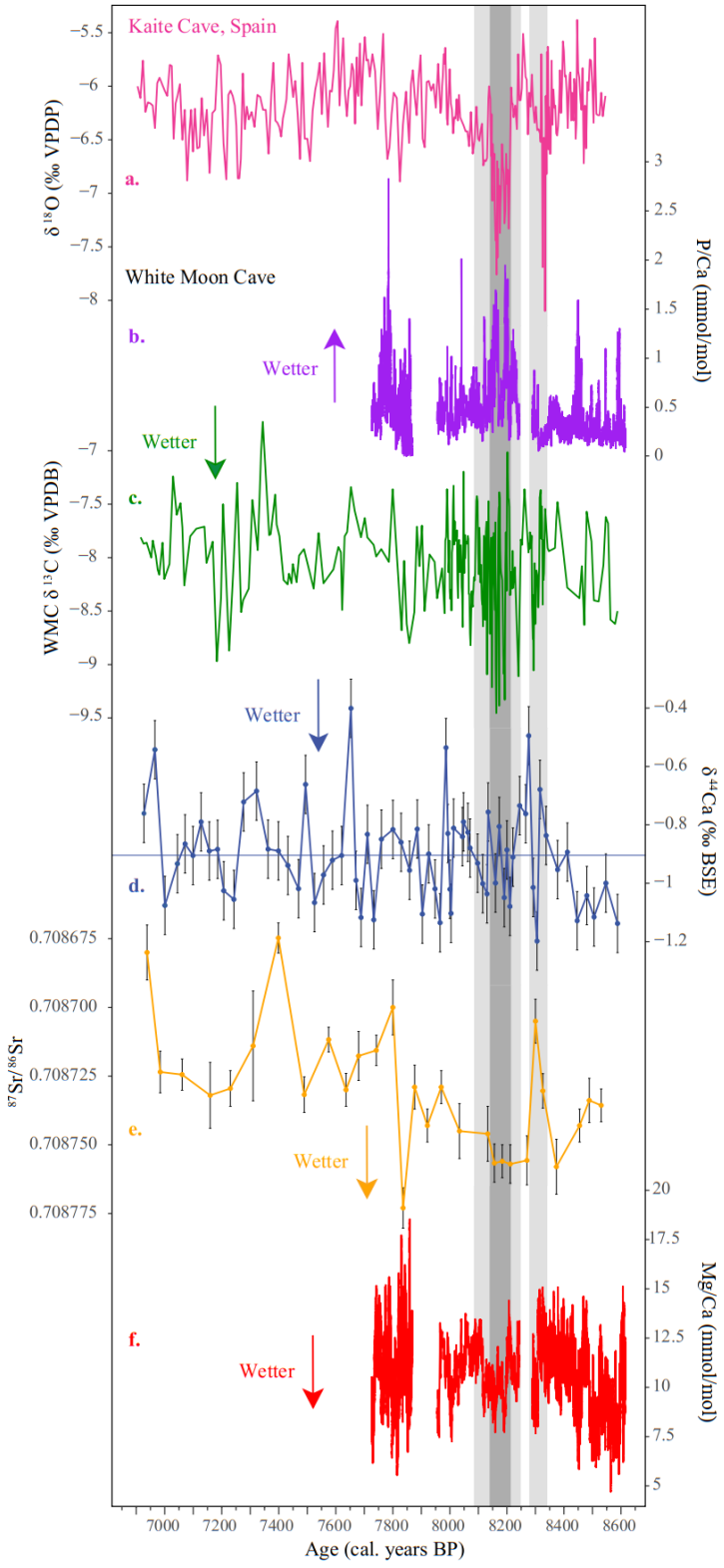

Figure 1. Speleothem δ18O for Kaite Cave, Spain (a; Dominguez-Villar, 2009), P/Ca (b), δ13C (c), δ44Ca(d), 87Sr/86Sr (e), and Mg/Ca (f) for WMC1. δ44Ca error bars show 2σ of the standard NIST915B over the analysis period (0.1‰). Blue line shows mean δ44Ca for WMC1. 87Sr/86Sr error bars represent

the 2σ uncertainty on the measurement (internal reproducibility). Dark and light gray shading show the central portion and entire duration of the 8.2kyr event after Thomas et al. (2007) and proposed precursor event at ~8300 yr cal BP.

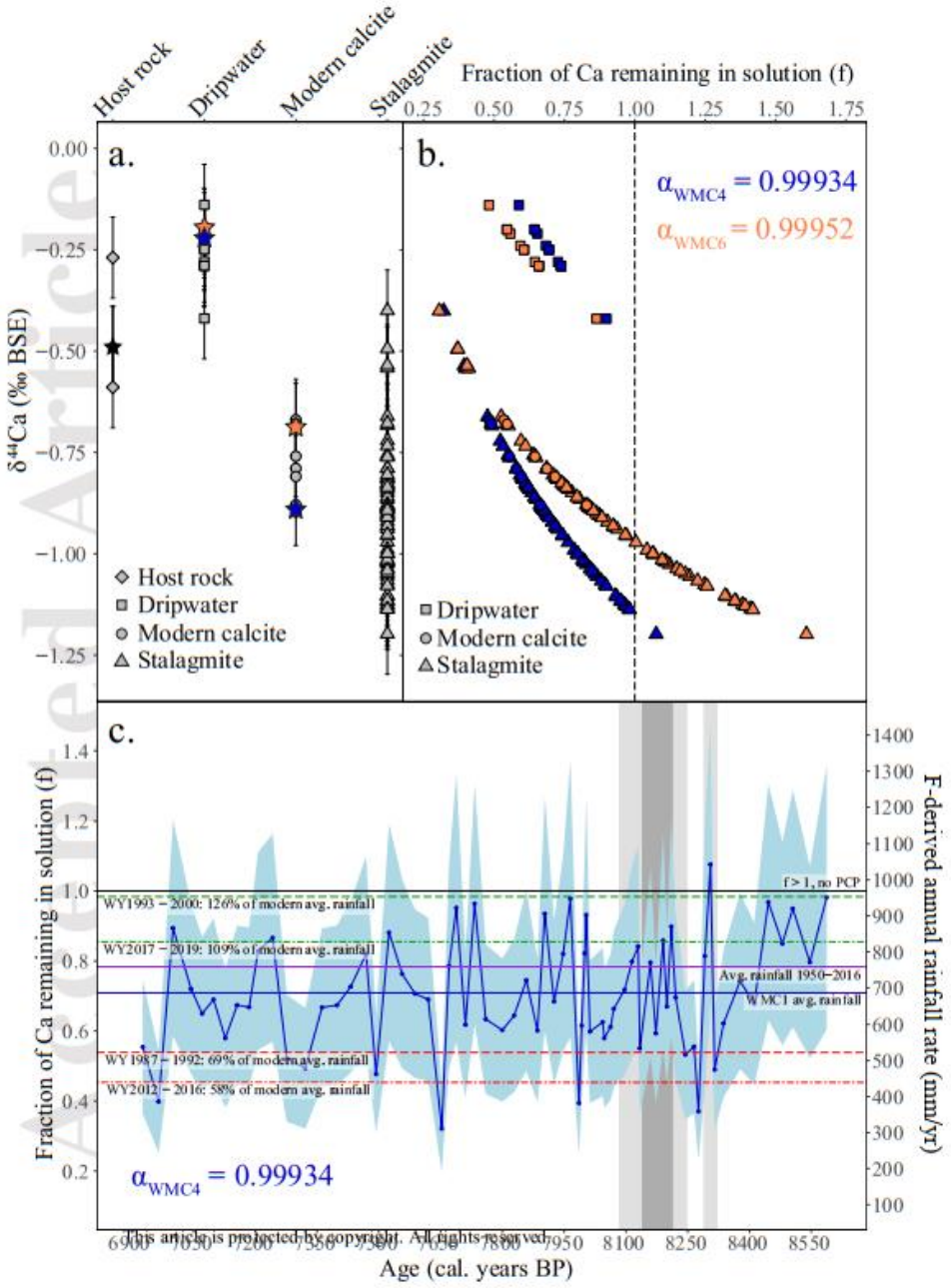

Figure 2. (a) δ44Ca values for WMC host rocks, dripwaters, modern calcite, and stalagmite WMC1. Stars denote median host rock (black) and mean dripwater and modern calcite for WMC4 (blue) and WMC6 (orange) used to calculate f values. (b) f values calculated using α values from drip site WMC4 (blue) or WMC6 (orange). (c) PCP reconstruction using equation 1 and αWMC4, and estimated rainfall rates. Uncertainty on f is analytical uncertainty on δ44Ca measurements propagated using a Monte Carlo

approach. f = 1 corresponds to a rainfall rate of ~969 mm/yr and represents a threshold above which theoretically no PCP occurs, and no specific rainfall rate can be estimated. Horizontal lines show average rainfall rates for Santa Cruz, CA: WMC1 stalagmite record (blue); annual (Jan. 1950–Jan. 2020) (purple); water year (WY: Oct. 1–Sept. 30) 1993–2000 (dashed green); WY 2017–2019 (two-dashed green); WY 1987–1992 (dashed red); WY 2012–2016 (two-dashed red).

12. 由生物调节的海气失衡驱动了冰期深海脱氧

翻译人：张亚南 zhangyn3@mail.sustech.edu.cn

Ellen Cliff, Samar Khatiwala,Andreas Schmittner. ***Glacial deep ocean deoxygenation driven by biologically mediated air–sea disequilibrium*** *[J].**Nature Geoscience**, 2021,14,43-50.*

https://doi.org/10.1038/s41561-020-00667-z

摘要：由各种指标推测出的深海脱氧，支持了冰期大气 CO2 含量的降低是因海洋生物泵加强的。这依赖于一种假设：表层海洋氧气（O2）与大气相平衡，深海中观察到的氧气缺乏都与有机物的降解消耗了 O2，以及产生溶解无机碳有关。但是，这种假设由于这种不平衡而具有瑕疵。我们使用了地球系统模型调谐到一系列的观测数据中，从而重现了指标记录中冰期—全新世氧化条件变化模式，以表明海气不平衡在冰期深海脱氧过程中扮演着重要角色。通过一种新的分解方法来追踪 O2，我们发现从前工业时期到最大冰盛期（LGM）整个海洋损失了 33Pmol O2，尽管其中 27Pmol 是由于温度降低导致的。这种损失是由生物调节的 02 不平衡所驱动，前工业时期对溶解平衡 O2 含量减少的贡献为 10%，在末次冰盛期为 27%。海冰和铁肥效应是末次冰盛期脱氧最大的贡献者，尽管冰期海洋中有机质的生产和降解都有所减少。我们的研究对冰期深海脱氧主要由于加强的生物泵作用或环流减缓造成的这一观点进行了挑战，并强调了 02 不平衡的重要性。

ABSTRACT: Deep ocean deoxygenation inferred from proxies has been used to support the hypothesis that a lower atmospheric carbon dioxide during glacial times was due to an increase in the strength of the ocean's biological pump. This relies on the assumption that surface ocean oxygen (O2) is equilibrated with the atmosphere such that any O2 deficiency observed in deep waters is a result of organic matter respiration, which consumes O2 and produces dissolved inorganic carbon. However, this assumption has been shown to be imperfect because of disequilibrium. Here we used an Earth system model tuned to a suite of observations, which reproduces the pattern of glacial-to-Holocene oxygenation change seen in proxy data, to show that disequilibrium plays an important role in glacial deep ocean deoxygenation. Using a novel decomposition method to track O2, we found a whole-ocean loss of 33 Pmol O2 from the preindustrial to the Last Glacial Maximum despite a 27 Pmol gain from the increased solubility due to cooler temperatures. This loss was driven by a

biologically mediated O2 disequilibrium, which contributed 10% of the reduction of the O2 inventory from the solubility equilibrium in the preindustrial compared with 27% during the Last Glacial Maximum. Sea ice and iron fertilization were found to be the largest contributors to the Last Glacial Maximum deoxygenation, which occurs despite overall reduced production and respiration of organic matter in the glacial ocean. Our results challenge the notion that deep ocean glacial deoxygenation was caused by a stronger biological pump or more sluggish circulation, and instead highlight the importance and previously underappreciated role of O2 disequilibrium.

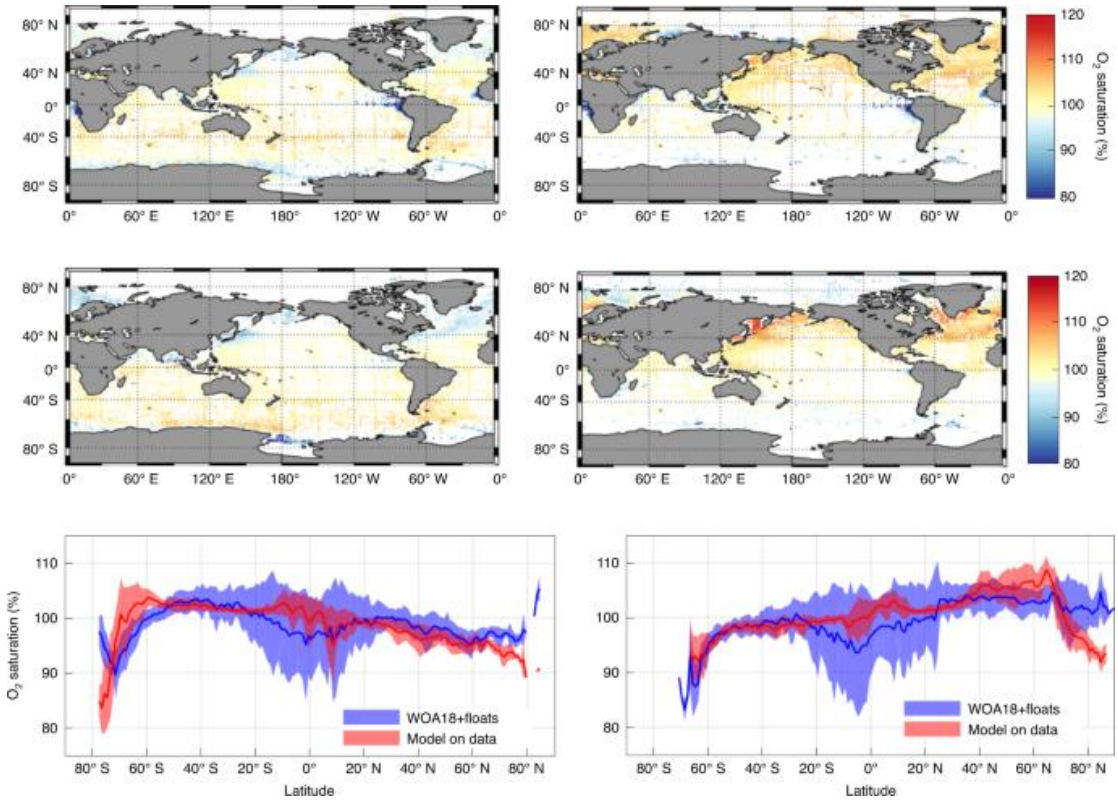

Figure 1. Comparison of surface O2 saturation from a compilation of the World Ocean Atlas 2018 (WOA18)+float data (University of Washington Argo O2 reanalysis, and quality-controlled data from the SOCCOM (Southern Ocean Carbon and Climate Observations and Modeling) programme). World Ocean Atlas 2018+float surface O2 saturation data (%) were spatially binned into 1 × 1° WOA grid boxes, and a seasonal climatology was made by binning data temporally by month (top row). Grid boxes without any measurements were discarded. Results shown here are for the Northern Hemisphere winter and Southern Hemisphere summer (December–January–February (DJF)) (left column), and the Northern Hemisphere summer and Southern Hemisphere winter (June–July–August (JJA)) (right column). Surface O2 saturation values are shown for observations (top row) and the model's PIC simulation interpolated to the locations where observations are available (middle row). The bottom row shows a comparison of

zonal mean surface O2 saturation in the observations and model at the location of observations, with one standard deviation of the zonal data shaded. Note that observations for the Southern Ocean are sparse, particularly in the winter months, as are those in the Arctic, where large model–data differences are seen and may be influenced by sampling biases in conditions without or with thin sea ice because research vessels are limited in accessing regions with thick sea ice cover.

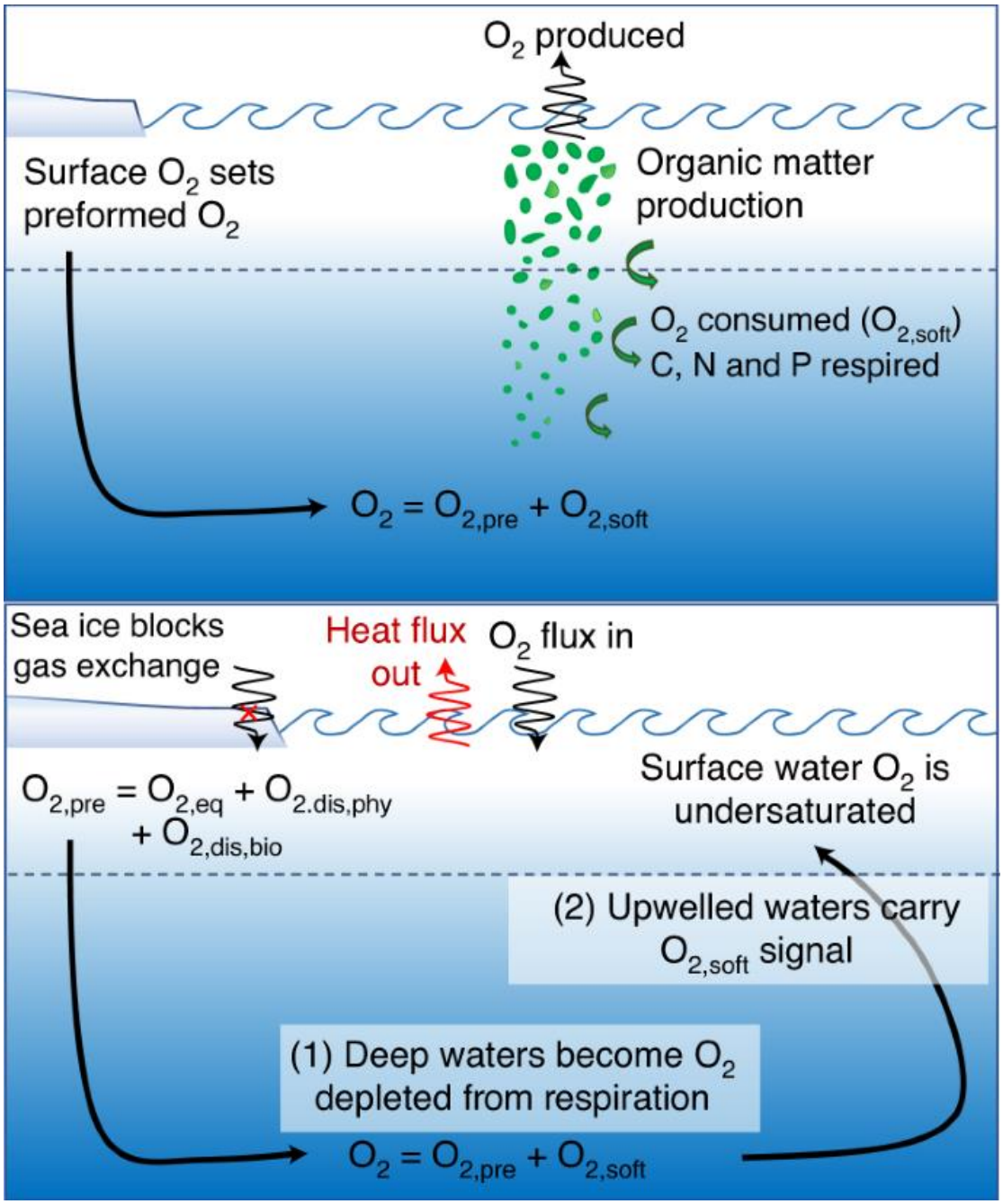

Figure 2. Schematic of the O2 decomposition used in this study. The top panel shows the standard decomposition (Methods) of O2 into preformed O2 (O2,pre), set at the surface and subsequently transported conservatively into the interior by the circulation, and O2,soft: O2 consumed during the

respiration of organic matter (which is therefore negative)14,18. The sum of these terms gives the total O2. The bottom panel shows the extended decomposition that incorporates surface disequilibrium, which causes deviation from the equilibrium preformed concentration (O2,eq). O2,dis,phy is caused by surface heat fluxes. Biological processes can also cause disequilibria (O2,dis,bio) by photosynthesis at the surface, which creates a positive disequilibrium, or as a result of the upwelling of waters depleted in O2 due to respiration, which leads to a negative disequilibrium. Waters upwelling in the Southern Ocean have a short surface exposure time so can have substantial O2,dis,bio, which may be enhanced by sea ice, which blocks gas exchange.

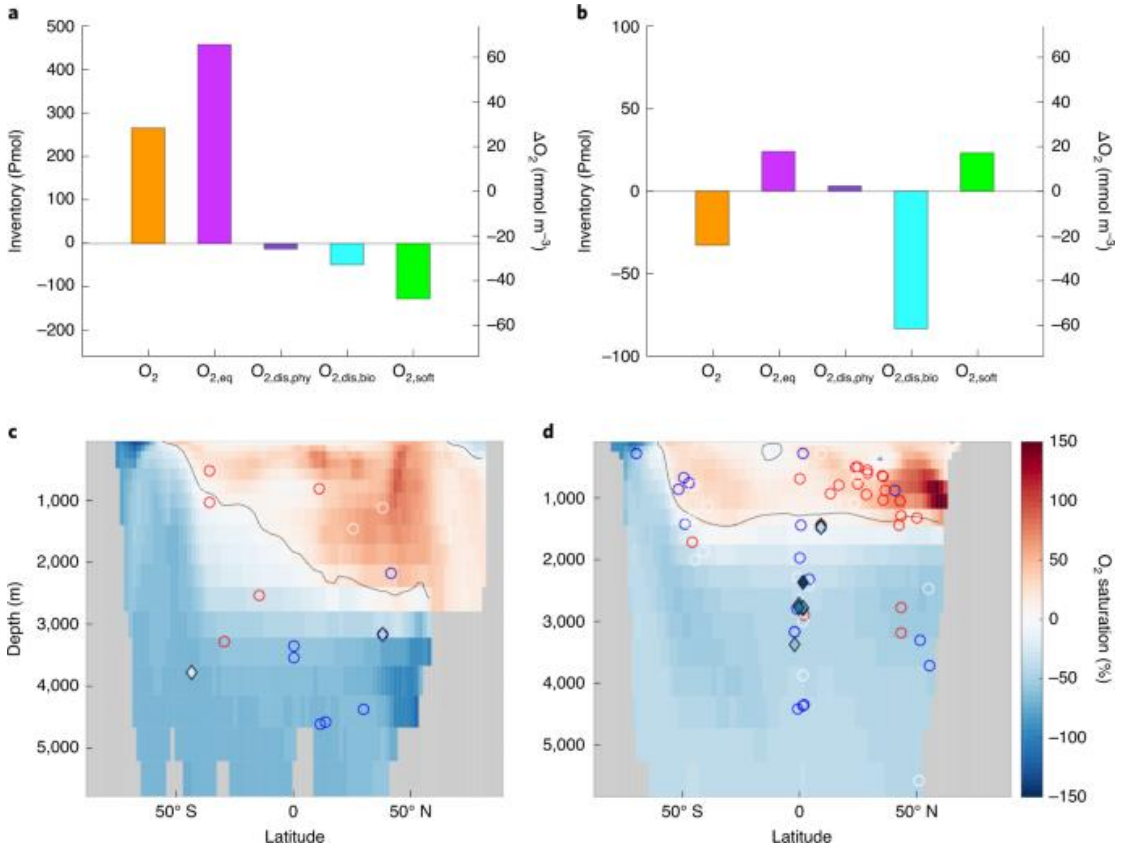

Figure 3. The components of O2 in the PIC and LGM relative to PIC. a,b, Oxygen decomposition for the PIC equilibrium simulation (a) and the difference between the LGM and PIC equilibrium simulations (b) are shown as inventory values. The equivalent deep ocean inventory decomposition plots are in Supplementary Fig. 5. c,d, Zonal mean sections of the LGM – PIC ΔO2 are shown for the Atlantic (c) and Pacific (d) oceans. Proxy-based reconstructions of ΔO2 from the LGM to the Holocene are included. Blue (red) circles indicate a qualitative decrease (increase) in O2 from the Holocene to the LGM. Diamonds represent a quantitative O2 change (mmol m–3) using results of the infaunal–epifaunal

foraminifera δ13C method that are within the range of a previously published calibration and are shaded according to the colour scale. The quantitative data point shown in the southern Atlantic was calculated using the modern O2 concentration at the core site as data were not available for the Holocene. See the Supplementary Information for further comparison of the model and reconstructions.

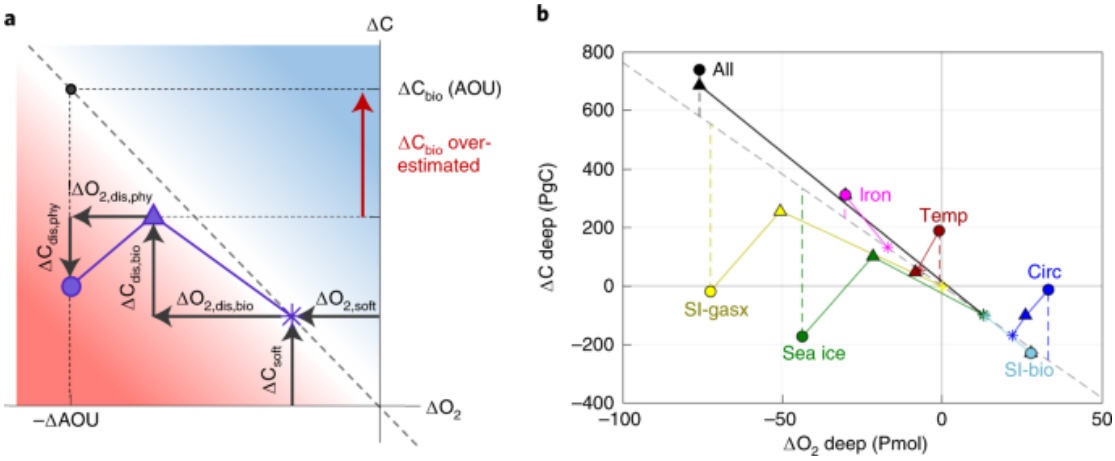

Figure 4. Relationship between ΔO2, ΔAOU and biological carbon storage. a, Schematic showing how the use of AOU can lead to an over- or underestimation of biological carbon storage. For a given ΔCbio (= ΔCsoft + ΔCdis,bio), the ratio of carbon to oxygen disequilibrium relative to the Redfield C:−O2 ratio (dashed grey line) controls whether AOU under- or overestimates the change in the true biological carbon storage. In a plot of ΔAOU versus ΔCbio, for points that plot in the red (blue) region below (above) the Redfield line, ΔCbio(AOU) over- (under-) estimates ΔCbio. Only for points that fall on the line does ΔCbio(AOU) accurately quantify the biological carbon storage change. Physical disequilibrium can cause further deviation from the Redfield line, which affects ΔAOU. b, ΔO2 versus ΔC in the deep ocean (below 1,000 m) for the perturbation experiments where an LGM condition is imposed on the preindustrial configuration. (For the relationship between the individual components, see Supplementary Fig. 25, and for reverse experiments with the PIC perturbations on the LGM state, see Supplementary Fig. 26). Changes are shown for the perturbations 'All' (black), sea ice (green), which is further separated into SI-gasx (yellow) and SI-bio (light blue), iron fertilization (pink), temperature (red) and circulation (dark blue). For each perturbation, three components of the carbon–oxygen system are shown: ΔO2,soft and ΔCsoft (stars), ΔO2,soft + ΔO2,dis,bio and ΔCbio (triangles) and the total O2 and C change from ΔAOU and ΔCbio + Δ Cdis,phy (circles).

13. 东亚季风中缺失的岁差带变化

翻译人：王浩森 11930841@mail.sustech.edu.cn

Clemens S C, Holbourn A, Kubota Y, et al. 2018. ***Precession-band variance missing from East Asian monsoon runoff****[J].* ***Nat Commun,*** *9: 3364.*

https:// DOI: 10.1038/s41467-018-05814-0

摘要：洞穴堆积物的 $CaCO_3$ $\delta^{18}O$ 是常用的古季风指标。但是，由于降水 $\delta^{18}O$ 的变化，温度影响以及在水汽输送路径上的降雨，根据浮游有孔虫的 $\delta^{18}O$ 推断局部降雨量可能会很复杂。这些可以通过长江流域（YRV）的浮游有孔虫 CaCO3 中的 $\delta^{18}O$ 来解决。优点是可以定量的去除全球海水 $\delta^{18}O$ 和局部温度变化的影响，从而得到了局部海水 $\delta^{18}O$ 的记录，该记录主要响应于局部降水和径流的稀释作用。 尽管长江流域的 $\delta^{18}O$ 由岁差（23 ky）周期控制，但局部海水 $\delta^{18}O$ 由偏心率（100 ky）和倾斜率（41 ky）周期控制，几乎没有岁差尺度的变化。这些结果与长江流域以外的记录一致，表明东亚季风降雨对温室气体和高纬度冰盖驱动比对直接日射驱动更敏感。

ABSTRACT: Speleothem CaCO3 δ18O is a commonly employed paleomonsoon proxy. However, inferring local rainfall amount from speleothem δ18O can be complicated due to changing source water δ18O, temperature effects, and rainout over the moisture transport path. These complications are addressed using δ18O of planktonic foraminiferal CaCO3, offshore from the Yangtze River Valley (YRV). The advantage is that the effects of global seawater δ18O and local temperature changes can be quantitatively removed, yielding a record of local seawater δ18O, a proxy that responds primarily to dilution by local precipitation and runoff. Whereas YRV speleothem δ18O is dominated by precession-band (23 ky) cyclicity, local seawater δ18O is dominated by eccentricity (100 ky) and obliquity (41 ky) cycles, with almost no precessionscale variance. These results, consistent with records outside the YRV, suggest that East Asian monsoon rainfall is more sensitive to greenhouse gas and high-latitude ice sheet forcing than to direct insolation forcing.

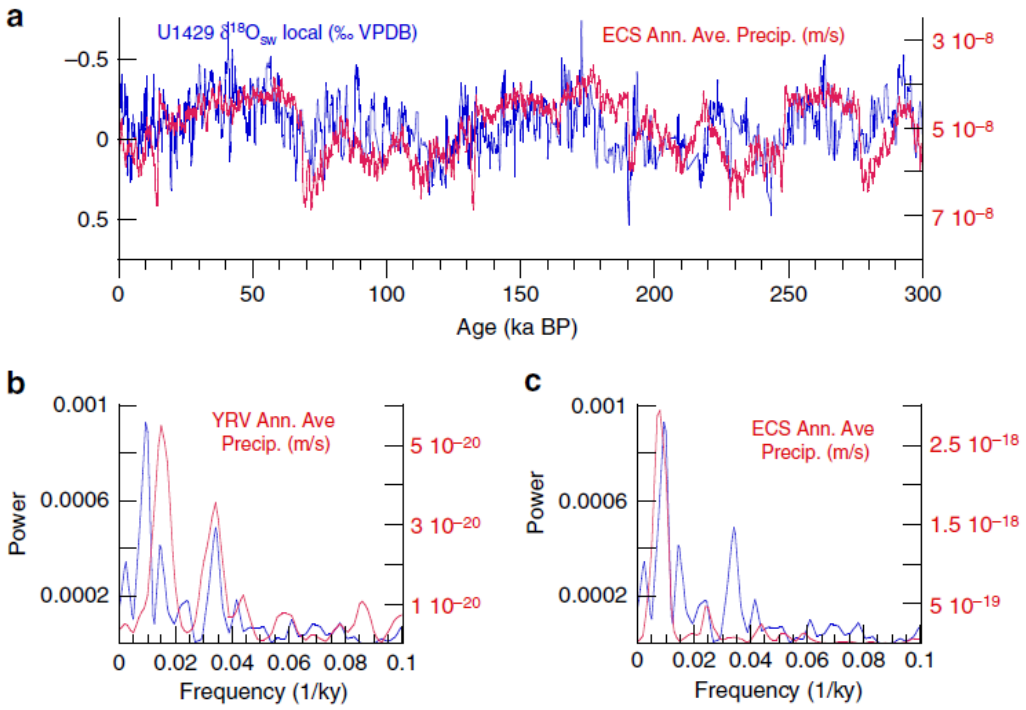

Figure 1. Comparison of model (annual average, red) and U1429 (blue) time series and spectra. **a** U1429 local $\delta^{18}O_{sw}$ and East China Sea (ECS) model annual average precipitation. The U1429 record is consistent with **b** annual average precipitation over the Yangtze River Valley (YRV) accounting for the 29- and 69-ky variance and **c** ECS annual average precipitation, accounting for the 100- and 41-ky variance. Supplementary Figure 6 shows comparisons of $\delta^{18}O_{cave}$ (for which temperature has not been removed) with model temperature and precipitation (monthly annual, maximum, and minimum)

14. 轨道驱动的季节日照变化对全新世亚非夏季风的影响

翻译人：郑威　11930589@mail.sustech.edu.cn

Wu C H, Tsai P C. ***Impact of orbitally-driven seasonal insolation changes on Afro-Asian summer monsoons through the Holocene****[J].* ***Communications Earth & Environment****, 2(1): 1-8.*

https://doi.org/10.1038/s43247-020-00073-8

摘要：理解是什么驱动了从陆地到海洋区域亚非夏季风的转变可以对理解气候动力、变化和模拟提供有用的价值。在这里，我们用数据模型分析来关注于全新世太阳辐射和季风对轨道变化的分化响应。我们发现，协同的、渐进式的夏季风季节性演化穿越了中全新世，说明中纬度急流是对流层上部的纽带。中全新世前，太阳辐射在夏季有显著性降低；大陆季风往东南向移动，与亚洲沿岸的季节性降水显著性增加一致。在夏季末，太阳辐射直到中全新世才有所减少。大陆季风的持续性减弱，加上太阳辐射减弱，迅速增加了东亚-西北太平洋的内在动力，加速了季风的大尺度迁移，表明轨道对季节变化的控制作用。

ABSTRACT: Understanding what drives a shift of the Afro–Asian summer monsoons from the continents to oceanic regions provides valuable insight into climate dynamics, changes, and modeling. Here we use data–model synthesis to focus on the differential seasonal responses of solar insolation and monsoons to orbital changes in the Holocene. We observe coordinated and stepwise seasonal evolution of summer monsoons across the mid-Holocene, suggesting the strengthening of the midlatitude jet stream as a bridge in the upper troposphere. Prior to the mid-Holocene, insolation had decreased considerably in early summer; the continental monsoons migrated southeastward, which corresponded to a more pronounced rainy season in coastal East Asia. In late summer, insolation did not decrease until the mid-Holocene. The continued weakening of the continental monsoons, combined with weakened insolation, rapidly enhanced the intrinsic dynamics over East Asia–Western North Pacific and accelerated a large-scale migration of the monsoon, suggesting orbital control of seasonal diversity.

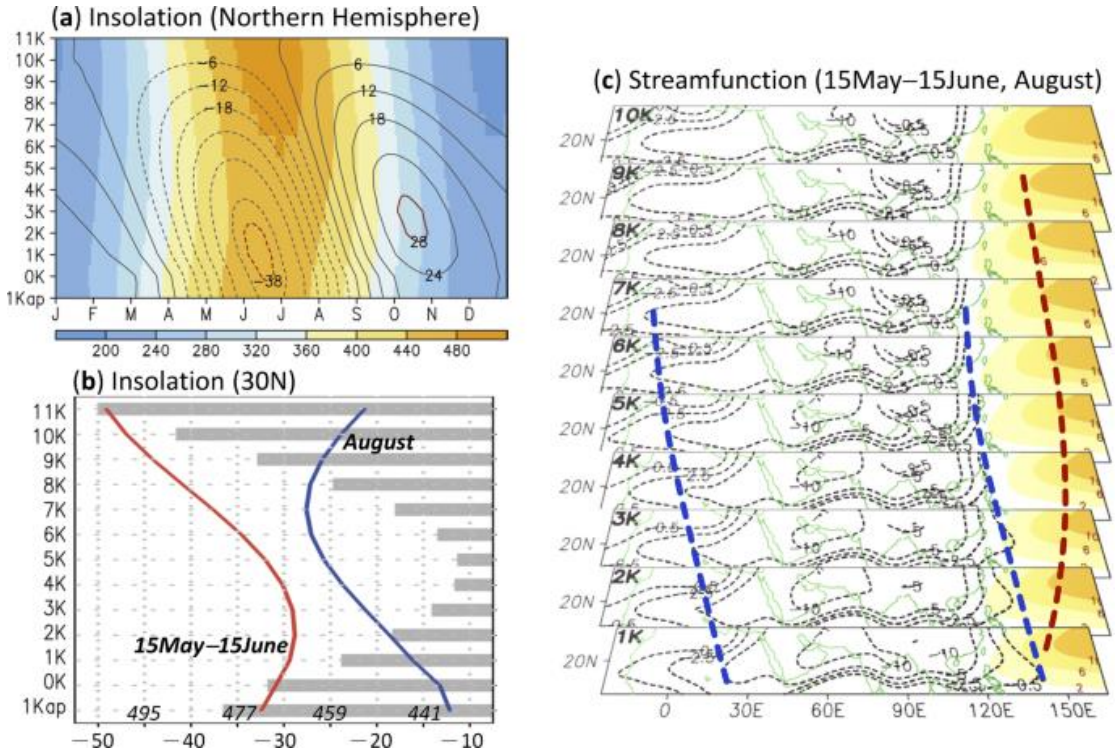

Figure 1. a Annual variation in the Northern Hemisphere insolation from 11 ka BP (11 K) to 1 ka after the present (1Kap) (shaded, unit: W m−2); contours denote that the insolation in 11 ka BP is subtracted. b Same as a except for averaged in 15 May–15 June (red line), August (blue line), and difference in between (gray bars) along 30°N. (c) Evolution of streamfunction at 850 hPa (unit: 106 m2 s−1) in 15 May–15 June (shaded, only for positive values) and August (contours, only for negative values) from 10 ka BP to 1 ka BP.

15. 从陨石古地磁研究太阳星云的历史

翻译人：张伟杰 12031188@mail.sustech.edu.cn

B. P. Weiss, X.-N. Bai, R. R. Fu, ***History of the solar nebula from meteorite paleomagnetism****.* ***Sci. Adv****. 7, eaba5967 (2021).*
https://doi.org/10.1126/sciadv.aba5967

摘要：我们回顾了我们对太阳星云和原行星盘的磁性理解的最新进展。我们讨论了理论、陨石测量和天文观测对了解行星形成和星云演化的意义。古地磁测量表明，在太阳系形成后，在距太阳约 1 至 3 个天文单位处存在 0.54±0.21 G 的磁场，在> 1.22 和> 2. 51 百万年距太阳 3∽7 AU 处存在≥0.06G 的磁场。这些磁场强度结果与预计能使典型的天文学观测到的原恒星堆积率达到∽$10^{-8}$$M_{\odot}$/年的强度一致，这表明磁力在原行星盘的质量转移中起了核心作用。古磁学研究还表明，太阳系内部和外部的磁场分别<0.006 G 和<0.003 G，在 3.94 和 4.89 Ma，这与此时散布的星云气体一致。这类似于太阳系外原行星盘的观测寿命。

ABSTRACT: We review recent advances in our understanding of magnetism in the solar nebula and protoplanetary disks (PPDs). We discuss the implications of theory, meteorite measurements, and astronomical observations for planetary formation and nebular evolution. Paleomagnetic measurements indicate the presence of fields of 0.54 ± 0.21 G at ~1 to 3 astronomical units (AU) from the Sun and ≥0.06 G at 3 to 7 AU until >1.22 and >2.51 million years (Ma) after solar system formation, respectively. These intensities are consistent with those predicted to enable typical astronomically observed protostellar accretion rates of ~10^{-8} $M_{\odot}$year−1, suggesting that magnetism played a central role in mass transport in PPDs. Paleomagnetic studies also indicate fields <0.006 G and <0.003 G in the inner and outer solar system by 3.94 and 4.89 Ma, respectively, consistent with the nebular gas having dispersed by this time. This is similar to the observed lifetimes of extrasolar protoplanetary disks.

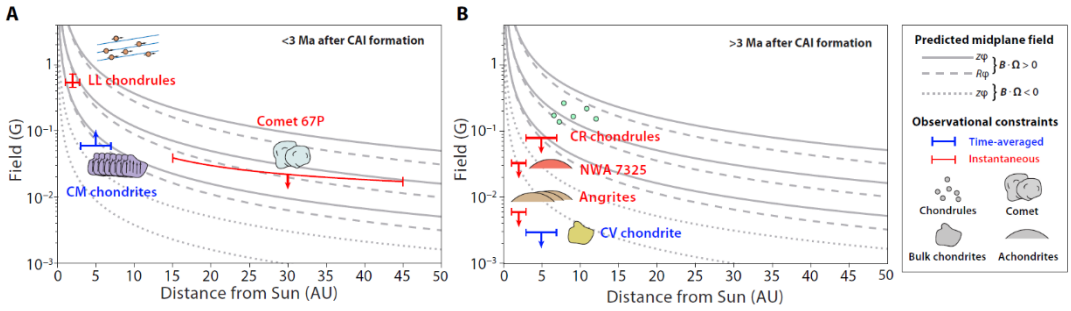

Figure 1. Paleomagnetic constraints on the nebular field as a function of distance from the young Sun. (A) Before 3 Ma after CAI formation. (B) After 3 Ma after CAI formation. Red and blue colors indicate instantaneous (red) and time-averaged (over >1 to 106 years) (blue) paleointensities, respectively, from LL (10, 155) and CR chondrules (160), bulk samples of CM chondrites (134), NWA 7325 (124), angrites (164), and a CV chondrite (163), and spacecraft measurements at comet 67P/Churyumov-Gerasimenko(171). Downward (upward) arrows indicate upper (lower) limits. Curves show the predicted midplane field assuming that magnetic stresses are driving accretion around a 1 $M_{\odot}$ star. Solid and dashed curves denote field assuming that the nebular field and sense of disk rotation are aligned, for which we assume contributions from both R (Eq. 2 with f = 50 and Lz ~ 6H) and z (dashed) (Eq. 3 with f' = 10 and taking m = 10) stresses, respectively. Dotted curves denote field assuming that the nebular field and sense of disk rotation are anti-aligned, for which we assume contributions from just the z stress (dashed) (Eq. 3 with f' = 10 and taking m = 1). For each case, fields are estimated for three assumed different accretion rates: 10^{-9}, 10^{-8}, and 10^{-7} $M_{\odot}$ year−1 (bottom, middle, and top curves). See tables S1 and S2 for source data.